A New Ionospheric Electron Precipitation Module Coupled with RAM-SCB within the Geospace General Circulation Model

Yiqun Yu[1], Vania K. Jordanova[2], Aaron J. Ridley[3], Jay M. Albert[4], Richard B. Horne[5], Christopher A. Jeffery[2]

[1] Space Science Institute, School of Space and Environment, Beihang University, Beijing, China

[2] Space Science and Application, Los Alamos National Laboratory, Los Alamos, New Mexico, USA

[3] Department of Atmospheric, Oceanic, and Space Sciences, University of Michigan, Ann Arbor, Michigan, USA

[4] Air Force Research Laboratory, Kirtland AFB, New Mexico, USA

[5] British Antarctic Survey, Cambridge, UK

Corresponding author: Y. Yu, Space Science Institute, School of Space and Environment, Beihang University, Beijing, China. (yiqunyu17@gmail.com)

This is the author manuscript accepted for publication and has undergone full peer review but has not been through the copyediting, typesetting, pagination and proofreading process, which may lead to differences between this version and the Version of Record. Please cite this article as doi: 10.1002/2016JA022585

Abstract. Electron precipitation down to the atmosphere due to wave-particle scattering in the magnetosphere contributes significantly to the auroral ionospheric conductivity. In order to obtain the auroral conductivity in global MHD models that are incapable of capturing kinetic physics in the magnetosphere, MHD parameters are often used to estimate electron precipitation flux for the conductivity calculation. Such an MHD approach however lacks self-consistency in representing the magnetosphere-ionosphere coupling processes. In this study we improve the coupling processes in global models with a more physical method. We calculate the physics-based electron precipitation from the ring current and map it to the ionospheric altitude for solving the ionospheric electrodynamics. In particular, we use the BATS-R-US MHD model coupled with the kinetic ring current model RAM-SCB that solves pitch angle dependent electron distribution functions, to study the global circulation dynamics during the January 25-26, 2013 storm event. Since the electron precipitation loss is mostly governed by wave-particle resonant scattering in the magnetosphere, we further investigate two methods of specifying electron precipitation loss associated with wave-particle interactions: (1) using pitch angle diffusion coefficients $D_{\alpha\alpha}(E, \alpha)$ determined from the quasi-linear theory, with wave spectral and plasma density obtained from statistical observations, (2) using electron lifetimes $\tau(E)$ independent on pitch angles inferred from the above diffusion coefficients. We found that both methods demonstrate similar temporal evolution of the trapped ring

current electrons, indicating that the impact of using different kinds of loss rates is small on the trapped electron population. However, for the precipitated electrons, the lifetime method hardly captures any precipitation in the large L-shell (i.e., $4 < L < 6.5$) region, while the diffusion coefficient method produces much better agreement with NOAA/POES measurements, including the spatial distribution and temporal evolution of electron precipitation in the region from the pre-midnight through the dawn to the dayside. Further comparisons of the precipitation energy flux to DMSP observations indicates that the new physics-based precipitation approach using diffusion coefficients for the ring current electron loss can explain the diffuse electron precipitation in the dawn sector, such as the enhanced precipitation flux at auroral latitudes and flux drop near the subauroral latitudes, but the traditional MHD approach largely overestimates the precipitation flux at lower latitudes.

1. Introduction

The ionospheric conductivity plays a key role in the magnetosphere-ionosphere coupled system because a major part of the conductivity is attributed to the magnetospheric dynamics and more importantly, it further controls a rich variety of magnetospheric processes. For instance, the aurora conductivity is associated with ionospheric electron precipitation in the auroral zone, which is closely related to plasma waves in the magnetosphere. On the other hand, the conductivity can greatly alter the ionospheric convection electric field that drives the transport of charged particles in the magnetosphere, controlling the source population to the ring current and radiation belts. Earlier studies have extensively explored the effect of the ionospheric conductivity on various magnetosphere-ionosphere processes, such as its temporal history [*Raeder et al.*, 1996], the substorm strength [*Raeder et al.*, 2001], the dawn-dusk asymmetry in the plasmasheet convection [*Lotko et al.*, 2014], the Cowling currents in the ionosphere [*Tang et al.*, 2011], and even the solar wind magnetosphere-ionosphere coupling [*Ohtani et al.*, 2014]. All these studies suggest that the ionospheric conductivity is a crucial but intricate element in the magnetosphere-ionosphere system, motivating deep investigation of its origin as well as its effect.

The ionospheric conductivity, as a result of ionization of the upper atmosphere, is created from several energy sources, including the solar EUV radiation, polar rain, nightside star light, and auroral particle precipitation. The auroral particle precipitation (associated with charged particles of $\sim$ 100 eV to tens of keV) originates from the magnetosphere

such that electrons/ions travel along magnetic field lines towards the Earth and collide with the neutral atmosphere.

The aurora is usually distinguished by two types of precipitation: discrete and diffuse aurora. Particles that generate discrete aurora are accelerated from their source regions in the magnetosphere and the corresponding electron precipitation, for example, is well correlated with the region of upward field-aligned currents. On the other hand, particles that are scattered by plasma waves into the loss cone can move down to the atmosphere along magnetic field lines without the aid of additional energy, creating diffuse auroral precipitation. There are two major candidates that are long believed to induce the diffuse auroral precipitation by pitch angle scattering the plasmasheet electrons: electromagnetic whistler-mode waves (e.g., hiss and chorus waves) and electrostatic electron cyclotron harmonic (ECH) waves [e.g., *Horne et al.*, 2003; *Ni et al.*, 2008]. While hiss waves are often identified inside the plasmasphere [*Meredith et al.*, 2004; *Cao et al.*, 2005; *Bortnik et al.*, 2009; *Laakso et al.*, 2015], chorus and ECH waves are excited in the near-Earth plasmasheet as well as in the nightside plasma trough region [e.g., *Meredith et al.*, 2001; *Wei et al.*, 2007; *Li et al.*, 2009; *Li et al.*, 2013], and only occasionally inside the plasmasheet [*Zhima et al.*, 2013]. Recent statistical analysis of years of satellite observations revealed that ECH waves dominantly contribute to the diffuse aurora in regions outside L shell of 8, whereas chorus waves are the main source of electron precipitation inside L shell of 8 [*Ni et al.*, 2011a; *Ni et al.*, 2011b; *Thorne et al.*, 2010]. These findings suggest that ECH waves are related with higher latitude diffusion precipitation, while the chorus wave scattering is mainly responsible for electron precipitation at the lower auroral latitudes.

Given these sources for the ionospheric auroral conductivity, first principle calculation of the conductivity is however not trivial in global models since it requires several important thermospheric-ionospheric characteristics, such as the chemistry, reaction rates, and electron/neutral density. To avoid the complexity of the thermosphere-ionosphere system, global models commonly adopt an empirical relation from *Robinson et al.* [1987] that links the precipitating energy flux and average energy to the Hall and Pedersen conductance (height-integrated conductivity) and thus significantly simplify the calculation of conductivity. Nevertheless, to utilize the Robinson's formula, one needs to, in the first place, provide electron precipitation flux at the ionospheric altitude. To obtain this kinetic quantity in global magnetohydrodynamics (MHD) models that are incapable of resolving the kinetic physics, researchers often use MHD parameters to approximate the kinetic precipitation flux at the ionospheric altitude [e.g., *Raeder et al.*, 2001; *Zhang et al.*, 2015]. Such estimate however does not reflect the physical mechanism in the magnetosphere-ionosphere coupled system because the real pitch angle scattering involves with kinetic-scale physics of the electrons, rather than fluid dynamics. Therefore a better approach, i.e., a physics-based calculation of electron precipitation flux is desired. For example, a kinetic ring current model that solves particle distribution functions with pitch angle dependence is among the leading candidates capable of providing the real precipitation flux. The flux is then further used to determine the ionospheric electrodynamics. Such a kinetic-scale connection between the ionosphere and magnetosphere has recently been established by *Fok et al.* [2014] in the Comprehensive Ring Current Model (CRCM) and *Chen et al.* [2015a, b] in the Rice Conveciton Model - Equilibrium (RCM-E) [*Lemon et al.*, 2004]. In this study, we step further from their stand-alone ring current models by de-

veloping an electron precipitation module within a geospace general circulation model in which the ring current model not only solves pitch angle dependent distribution functions but also is coupled to a global MHD model. While the former feature yields a more physical representation of the electron distribution, the latter introduces more self-consistency than a stand-alone regional model that relies on various external boundary conditions [*Yu et al.*, 2014a].

Figure 1 (a) illustrates the general coupling structure within a global circulation modeling framework. The ionospheric potential solver takes parameters from the global MHD model such as field-aligned currents $J_{||}$, and calculates the ionospheric conductance Σ and electric potential Φ. The typical technique of calculating the auroral conductance is the empirical Robinson's formula, which relates the conductance with electron precipitation energy flux E and average energy at the ionospheric altitude. According to adiabatic kinetic theory, the electron precipitation flux F_e, is approximated using MHD parameters such as electron temperature, density, and field-aligned currents [*Knight*, 1973; *Fridman and Lemaire*, 1980; *Zhang et al.*, 2015]. This approach, as discussed above, cannot truly represent the physics-based electron precipitation in the coupling regime that actually requires kinetic-scale physics. Hence in this study we replace this MHD parameterized calculator with a physics-based method, as shown in Figure 1 (b). Since the kinetic ring current model solves pitch angle dependent distribution functions of electrons and takes into account electron loss mechanisms associated with wave-particle pitch angle scattering, the electron precipitation can be determined by integrating the electron flux within the loss cone and then mapped down to the ionospheric altitude for the calculation of conductivity. This method follows the physical coupling processes and therefore estab-

lishes, in the modeling framework, a more physics-based module of the ionospheric auroral conductivity.

Within those stand alone ring current models, earlier studies on ring current electron dynamics [e.g., *Jordanova et al.*, 2010; *Fok et al.*, 2014; *Chen et al.*, 2015a, b] often use electron lifetimes to account for the loss process due to wave-induced scattering. The lifetimes represent the relaxation time of electrons before they are lost due to various loss mechanisms, and is simple and in many circumstances applicable when pitch angle dependence is weak, because the lifetimes imply the decay of the distribution as a whole at all pitch angles. Methods of calculating the electron lifetimes [e.g., *Albert and Shprits*, 2009] has been validated and improved in the past decade and found to be a very good approximation to the exact lifetime [e.g. *Artemyev et al.*, 2013], and thus being extensively and successfully employed in radiation belt studies [e.g., *Ripoll et al.*, 2014, 2015, 2016; *Artemyev et al.*, 2015; *Mourenas et al.*, 2012a, b, 2014; *Yu et al.*, 2013; *Yu et al.*, 2014b]. In the ring current dynamics, the effect of using different electron loss models (i.e., different electron lifetimes) has been recently investigated by *Chen et al.* [2015b] in the RCM-E model. It is found that the MLT and Kp parameterized loss rates, associated with chorus and hiss wave scattering in the inner magnetosphere, lead to a much better performance than other static and simple electron loss models after comparing the simulation results with LANL/GEO trapped electron flux and NOAA/POES precipitated flux. Their new loss model uses electron lifetimes provided by *Orlova and Shprits* [2014] and *Orlova et al.* [2014] for the chorus and hiss wave scattering outside and inside the plasmapause, respectively. These lifetime are inferred, following methods described in *Albert and Shprits* [2009], from pitch angle diffusion coefficients determined from statistical observations of

wave properties and parameterized with Kp index and MLT sectors [*Orlova and Shprits*, 2014; *Orlova et al.*, 2014]. They are independent on pitch angles and are suitable to be used in the RCM-E model that solves isotropic electron distributions.

While the method of calculating lifetimes in *Albert and Shprits* [2009] and others gives a very good approximation to the exact lifetime, the latter does not always lead to a good approximation to using the pitch angle diffusion coefficients, especially when considering pitch angle and local time dependence or during transient phase before the distribution is settled down. Therefore, when the particle distribution is anisotropic (which is common during storms/substorms) or its gradient near the edge of loss cone is pronounced or the relaxation time is longer than the loss timescale, it might not be quite rational to use lifetime for the wave-induced scattering. Therefore a more comprehensive way is required, such as considering the pitch angle dependent diffusion coefficient. For example, *Jordanova et al.* [2008] treated the pitch angle scattering due to EMIC waves as a diffusive process in the RAM-SCB ring current model by using pitch angle diffusion coefficients. Those coefficients carry full pitch angle information for diffusing the ring current particles and potentially offer a more appropriate approach to taking fully into account the precipitation loss associated with waves. This can further yield better representation of ionospheric conductivity.

In this study we will investigate both methods: (a) use pitch angle diffusion coefficients to represent wave particle scattering loss (refer to as "diffusion coefficient method" hereafter) and (b) use electron lifetimes (refer to as "lifetime method" hereafter). With the new implementation shown in Figure 1(b), this study aims to 1) validate and assess the fidelity and capability of the new modeling framework in resolving the ionospheric

electron precipitation, 2) compare two electron loss methods in including the effect of wave-induced scattering on electron dynamics, and 3) understand the wave-induced auroral electron precipitation and its influence on the magnetosphere-ionosphere dynamics. The paper is structured as follows. In section 2 we will describe the new coupling framework, especially two important components in the framework: the electron precipitation loss associated with wave resonant pitch angle scattering, and the auroral conductivity. In section 3 we report results from three simulations using these different methods and then compare with observations. In section 4 we conclude.

2. Methodology

In this study, the Space Weather Modeling Framework (SWMF) [*Tóth et al.*, 2005, 2012] is used to study the electron precipitation. The framework is composed of several inter-coupled physical models, from global magnetosphere to regional representation inside the magnetosphere, as shown in Figure 1 (c). The global MHD model BATS-R-US (Block Adaptive Tree Scheme-Roe type-Upstream) [*Powell et al.*, 1999] solves single-fluid ideal MHD equations for the whole magnetospheric dynamics. The kinetic ring current model RAM-SCB (Ring current-Atmosphere interaction Model with Self-Consistent Magnetic field (B)) [*Jordanova et al.*, 2006, 2010; *Zaharia et al.*, 2006, 2010] is described by bounce-averaged Fokker-Planck equations inside the geosynchronous altitude. The ionospheric potential solver RIM [*Ridley et al.*, 2004] is designated as a two dimensional shell at the ionospheric height (∼110 km). The coupling between these codes, except for the dashed line between RAM-SCB and RIM, has been established in previous studies and meanwhile been validated through thorough comparisons with a variety of observations, including the global energy content Dst index, magnetic fields, field-aligned currents, and particle flux

either at the boundary of codes or along certain satellites trajectories [*Zaharia et al.*, 2010; *Yu et al.*, 2014a, 2015; *Welling et al.*, 2011; *Welling et al.*, 2015]. These data-model comparisons for this coupled modeling framework demonstrated its capability to reproduce many key features of the magnetosphere-ionosphere system. Similar abilities are also achieved in other types of MHD-kinetic coupled models, such as LFM-RCM [*Pembroke et al.*, 2012], BATS-R-US-RCM [*De Zeeuw et al.*, 2004], and BATS-R-US-CRCM [*Glocer et al.*, 2013].

In our coupled modeling framework shown in Figure 1 (c), the MHD model BATS-R-US provides plasma density and temperature to the RAM-SCB model at its outer boundary of 6.5 R_e in the equatorial plane. An isotropic Kappa distribution (κ=3) is assumed using the MHD temperature and density. The flux from the single-fluid MHD model is further decoupled into individual plasma compositions needed in RAM-SCB by employing the empirical relationship from *Young et al.* [1982] who correlated the plasma sheet ion composition with solar wind and magnetospheric conditions. In turn, the RAM-SCB model passes the equatorial ring current pressure to the MHD model, in order to compensate the pressure deficiency in the MHD code since the latter lacks kinetic physics and is unable to capture the westward/eastward particle drift physics. In the MHD model, the pressure is gradually "nudged" toward, instead of forced to the ring current pressure to avoid potential numerical instability, following the approaches in *De Zeeuw et al.* [2004] and *Glocer et al.* [2013]. The "nudging" is achieved with the expression:

$$P'_{MHD} = P_{MHD} + min(1, \frac{dt}{\tau_{couple}}(P_{RAM-SCB} - P_{MHD})) \quad (1)$$

where P_{MHD} and P'_{MHD} are the MHD pressure before and after coupling, respectively. τ_{couple} is a time constant introduced to maintain solution stability and it is 60 seconds in this study. Therefore the MHD pressure is converged toward the RAM-SCB pressure $P_{RAM-SCB}$ after $2\tau_{couple}$.

The ionospheric potential solver computes the electric potential calculation using field-aligned currents from the MHD model and Hall/Pedersen conductance. The electric potential is then mapped out along magnetic field lines to the magnetosphere assuming zero potential drop along magnetic field lines. In the BATS-R-US model, the electric potential is used to specify the velocity of the footprints of magnetic field lines on its inner boundary (at 2.5 R_e), while the RAM-SCB model uses the corresponding convection electric field to drive charged particles around the Earth. The inductive electric field is not included in the ring current model, as it has been found by *Zaharia* [2008] that the inductive electric field is generally much smaller than the convection electric field inside the geosynchronous orbit, but can be comparable during late main phase/early recovery phase at some local times, suggesting its localized feature [*Ganushkina et al.*, 2013]. The magnetic field required at the outer boundary of RAM-SCB is provided by the empirical Tsyganenko model [*Tsyganenko*, 1989], parameterized by Kp index. Since the magnetic field solver within RAM-SCB represents the field with a set of Euler potential shells [*Zaharia et al.*, 2006, 2010], it is difficult to construct the shells at the outer boundary with fields from other coupled code [*Welling et al.*, 2015].

In the following sections, two key components of the framework are described in detail: (a) the auroral electron precipitation of magnetospheric origin in the RAM-SCB in Section 2.1 and (b) the ionospheric conductance in Section 2.2. We will firstly describe the

ring current model RAM-SCB and two loss methods used to give rise to the wave-induced electron precipitation, namely the diffusion coefficient method and lifetime method (Section 2.1.1). Then in Section 2.2.1 we will describe the traditional MHD approach in determining the precipitation for the ionospheric conductance, and in Section 2.2.2 the physics-based approach by using the wave-induced precipitation flux.

We conduct three simulations listed in Table 1: (1) using the physics-based calculation of auroral precipitation with the diffusion coefficient method in the ring current model, (2) using the physics-based calculation of auroral precipitation with the lifetime method in the ring current model, and (3) using MHD approximation for the auroral precipitation where the precipitation flux is not determined from the ring current model, but rather from the MHD model (i.e., Figure 1.

2.1. Magnetospheric electron precipitation in the RAM-SCB model

The RAM-SCB model includes two fully coupled modules: a kinetic ring current-atmosphere interaction model (RAM) [*Jordanova et al.*, 1994, 2006, 2010] self-consistently (SC) coupled with a 3D equilibrium magnetic field (B) code [*Zaharia et al.*, 2006, 2010]. It has been validated via a variety of space-borne observations and geomagnetic indices [*Yu et al.*, 2012]. The model determines the magnetic field configuration in three dimensions and the particle distribution functions $Q_l(R, \phi, E, \alpha)$ from bounce-averaged Fokker-Planck equations for both ring current ions and electrons in the equatorial plane:

$$\frac{\partial Q_l}{\partial t} + \frac{1}{R_o^2}\frac{\partial}{\partial R_o}(R_o^2 < \frac{dR_o}{dt} > Q_l) + \frac{\partial}{\partial \phi}(< \frac{d\phi}{dt} > Q_l)$$
$$+\frac{1}{\gamma p}\frac{\partial}{\partial E}(\gamma p < \frac{dE}{dt} > Q_l) + \frac{1}{h\mu_o}\frac{\partial}{\partial \mu_o}(h\mu_o < \frac{d\mu_o}{dt} > Q_l)$$

$$= < (\frac{\partial Q_l}{\partial t})_{loss} > \quad (2)$$

where Q_l is a function of radial distance R from 2 to 6.5 R_e with spatial resolution of 0.25 R_e, geomagnetic east longitude ϕ with resolution of 15°, energy E between 0.15 to 400 keV, and pitch angle α from 0 to 90°. The bracket <> represents bounce averaging, the subscript index o denotes the equatorial plane, p is the relativistic momentum of the particle, γ is the relativistic factor, and h is defined by:

$$h(\mu_o) = \frac{1}{2R_0} \int_{s_m}^{s_m'} \frac{ds}{\sqrt{(1 - B(s)/B_m)}} \quad (3)$$

which is proportional to the bounce period. Here, B_m is the magnetic field at the mirror point, ds is a distance interval along the integrating field line, and R_0 is the equatorial distance of the field line.

The loss terms on the right hand side of Equation (2) are represented by several physical processes, including charge exchange with geocoronal hydrogen for ring current ions, atmospheric collisional loss for both electrons and ions, and pitch angle scattering of electrons due to wave particle resonance that eventually leads to the diffuse auroral precipitation [*Jordanova et al.*, 2010]. The diffuse aurora has long been believed to be associated with electron precipitation induced by wave-particle interactions in the magnetosphere, such as whistler mode chorus and ECH waves. Recent quantitative studies found that whistler mode chorus waves play a dominant role over the ECH waves in scattering plasmasheet electrons from a few hundred eV to tens of keV in the inner magnetosphere down to the auroral zone, producing intense diffuse auroral precipitation [*Thorne et al.*, 2010; *Ni et al.*,

2011a; *Ni et al.*, 2011b]. Therefore the effect of ECH waves on the electron precipitation is excluded in the ring current model RAM-SCB for this study.

2.1.1. Electron precipitation loss method used in RAM-SCB

To include the contribution of wave particle interactions to the loss term in Equation (2), we describe two loss methods as follows:

1. The "diffusion coefficient method" uses pitch angle diffusion coefficients $D_{\alpha\alpha}(E,\alpha)$ and solves the pitch angle diffusion equation with a Crank-Nicolson scheme [*Jordanova et al.*, 1996; *Jordanova et al.*, 1997; *Jordanova et al.*, 2008] for the loss term $< (\frac{\partial Q_l}{\partial t})_{loss} >$ in Equation (2):

$$< (\frac{\partial Q_l}{\partial t})_{WPI_{loss}} >= \frac{1}{h\mu_o}\frac{\partial}{\partial \mu_o}\left[h\mu_o < D_{\mu_o\mu_o} > \frac{\partial Q_l}{\partial \mu_o}\right]$$
$$< D_{\mu_o\mu_o} >= (1-\mu_o^2) < D_{\alpha\alpha} > \quad (4)$$

where $< D_{\alpha\alpha} >$ ($\mu_o = cos(\alpha_o)$) is bounce-averaged pitch angle diffusion coefficients associated with whistler-mode chorus and hiss waves, and α_o is the equatorial pitch angle. The coefficients associated with chorus wave scattering are determined from quasi-linear theory using the PADIE code [*Glauert and Horne*, 2005; *Horne et al.*, 2013; *Glauert et al.*, 2014], based on statistical observations of wave properties for regions outside the plasmapause. In particular, they were derived based on wave frequency spectra and frequency ratio (f_{pe}/f_{ce}) parameterized from satellite observations for $1.5 \leq L^* \leq 10$, magnetic latitude $0° \leq \lambda_m \leq 60°$ and five levels f Kp. To be used in the above equation, they are then interpolated onto RAM-SCB energy, pitch angle, as well as spatial grids On the other hand, precipitation due to hiss wave scattering inside the plasmapause is consid-

ered by using hiss wave pitch angle diffusion coefficients computed from a similar code [*Albert*, 2005]. These coefficients all depend on plasma density, energy, and pitch angle, representing a comprehensive scattering of ring current electrons.

2. The "lifetime method" uses electron lifetimes to include the loss effect of wave-particle interactions in Equation (2):

$$< (\frac{\partial Q_l}{\partial t})_{WPI_{loss}} >= -(\frac{Q_l}{\tau}) \quad (5)$$

The lifetimes τ are computed from the above diffusion coefficients $D_{\alpha\alpha}(E, \alpha)$ using the method described in *Albert and Shprits* [2009]. The coefficients are integrated at the lowest normal mode over all pitch angles and local times, leading to lifetimes independent on MLT and pitch angles. The lifetimes are also categorized into two kinds: one due to chorus wave scattering outside the plasmapause and the other due to hiss wave scattering inside. These time scales are interpolated onto RAM-SCB energy grid assuming pitch angle isotropic and vary in radial distance and storm activity level (for more details see *Jordanova et al.* [2010]). It should be noted that these lifetimes differ from empirical lifetimes [e.g., *Chen and Schulz*, 2001; *Albert*, 1999] that represent the total decay time, regardless of the associated waves behind.

Once the electrons are "scattered" in the loss cone corresponding to the ionospheric altitude of 200 km, the electron precipitation flux is calculated by integrating the electron distribution function within the loss cone, as will be described in the next section. The precipitation removal of the ring current electrons is calculated with a time scale of a quarter bounce period [*Jordanova et al.*, 2008].

2.2. Ionosphere conductance

The ionospheric electrodynamics is solved over a spheric shell at 110 km above the Earth surface. This shell is connected with the magnetosphere models mainly via field-aligned currents and mapping electric potential. The ionospheric electric potential Φ is governed by the field-aligned currents $J_{||}$ and height-integrated conductance Σ:

$$\nabla \cdot (\Sigma \cdot \nabla \Phi) = -J_{||} \sin I \tag{6}$$

where Σ is the tensor of ionospheric conductance, including both Hall and Pedersen conductance, and I is the inclination of the magnetic field line at the ionosphere.

The ionospheric conductance is induced by several physical processes, including diffuse auroral precipitation, discrete auroral precipitation, solar EUV radiation, and polar rain. They are all included in the ionospheric electrodynamics model:

$$\Sigma = \sqrt{\Sigma^2_{diffuse} + \Sigma^2_{discrete} + \Sigma^2_{EUV} + \Sigma^2_{polarrain} + \Sigma^2_{nightside}} \tag{7}$$

The conductance associated with solar EUV radiation is calculated using an empirical function based on the solar zenith angle and f10.7 index [*Moen and Brekke*, 1993]. To include the weak contribution from polar rain, small background conductance is applied constantly and uniformly over the polar cap above the open/closed field line boundary. In addition, aurora conductance is obtained using Robinson's empirical formulas [*Robinson et al.*, 1987] provided the energy flux F_E and average energy $\overline{E}$ of the electron precipitation at the ionospheric altitude:

$$\Sigma_P = \frac{40\overline{E}}{16 + \overline{E}^2}\sqrt{F_E}$$
$$\Sigma_H = 0.45\overline{E}^{0.85}\Sigma_P \quad (8)$$

These expressions are approximate fits to the the conductivity values obtained by *Vickrey et al.* [1981] based on energy deposition functions given by *Rees* [1963] in the altitude range 80 - 200 km. Although these expressions assume a Maxwellian distribution in energy, they have been shown to work well for non-Gaussian distribution if the correct average energy and energy flux are used [*Robinson et al.*, 1987]. These relations, as mentioned earlier, have been widely employed in global magnetosphere models [e.g., *Ridley et al.*, 2004; *Raeder et al.*, 2001; *Zhang et al.*, 2015; *Fok et al.*, 2014; *Chen et al.*, 2015a].

Although both diffuse precipitation and discrete aurora precipitation utilize the above relations, they are categorized into two different precipitation mechanisms. While diffuse aurora originates from precipitating electrons that are scattered into the loss cone, the discrete aurora is associated with electrons that are accelerated towards the Earth aided by electric potential difference along magnetic field lines. To numerically evaluate these two types of aurora conductance using Equation (8), the energy flux F_E is determined separately. The numerical implementation of these two types of auroral precipitation in global circulation models is described below in detail. Two approaches are investigated: One is the traditional MHD parameterization, and the other one with a coupled kinetic ring current model is based on physical precipitation process. These two approaches are already illustrated in Figure 1 (a, b).

2.2.1. MHD approach

In global MHD models, a common way of specifying the auroral electron precipitation follows the adiabatic kinetic theory in *Knight* [1973]; *Lyons et al.* [1979]; *Fridman and Lemaire* [1980] using MHD parameterization [e.g., *Raeder et al.*, 2001; *Tanaka*, 2000; *Zhang et al.*, 2015]. We describe the precipitation method in *Zhang et al.* [2015] as an example of the MHD approach. In their study, the number flux of electron precipitation in the source region F_0 is firstly determined from the adiabatic kinetic theory:

$$F_0 = \beta \frac{N_e T_e^{1/2}}{\sqrt{2\pi m_e}} \tag{9}$$

where T_e, N_e are the electron thermal temperature and electron number density at the source region in the magnetosphere. The electron temperature is assumed to be 1/6 of the proton temperature in the MHD model based on typical observations in the plasmasheet. Such a ratio of 1/6 is a crude approximation though; since this simple relationship is probably only valid for low energy plasmasheet particles in the near-Earth region, a better representation between the electron and proton temperature is desired. The electron number density is assumed to be equal to the proton number density from the MHD model. β represents the filling rate of loss cone from the plasmasheet, and is chosen to be 0.5 for simplicity in this study. Future investigation should take into account its spatial variation for more comprehensive and realistic consideration, as demonstrated in *Zhang et al.* [2015].

For the diffuse precipitation, the energy flux F_E and averaged energy E use the following expressions:

$$F_E = 2F_0T_e$$

$$< E >= 2T_e \tag{10}$$

For discrete electron precipitation that is related to the upward field-aligned currents, its energy flux is modeled as:

$$F_E = \frac{J_{||}}{e}\left[2T_e + eV\frac{1-e^{-eV/T_e(R_m-1)}}{1+(1-1/R_m)e^{-eV/T_e(R_m-1)}}\right]$$

$$E = 2T_e + eV\frac{1-e^{-eV/T_e(R_m-1)}}{1+(1-1/R_m)e^{-eV/T_e(R_m-1)}}$$

$$eV = T_e(R_m-1)ln\frac{R_m-1}{R_m-j_{||}/eF_0} \tag{11}$$

where $J_{||}$ is the field-aligned current, and R_m is the ratio of magnetic field between the ionospheric footprint and the equatorial location. eV acts as the energy source to accelerate electrons from the equator towards the Earth as these electrons themselves have insufficient initial energy to reach the atmosphere. These calculation is only applied to regions of upward field-aligned currents.

2.2.2. Physics-based approach

With a ring current code RAM-SCB coupled into the geospace general circulation model. the energy flux of diffuse aurora precipitation $F_E^{diffuse}$ is computed from the equatorial flux distribution j_o obtained from the RAM-SCB model. First, the averaged electron precipitation flux inside the loss cone $\overline{j_{oc}}$ in the equatorial plane is:

$$\overline{j_{oc}(E)} = \frac{\int_{\mu_{oc}}^{1} d\mu j_o(E,\mu)}{\int_{\mu_{oc}}^{1} d\mu_o} \tag{12}$$

where $\mu_o = cos(\alpha_o)$ and α_o is the equatorial pitch angle, j_o is the electron differential flux distribution in the equatorial plane and μ_{oc} is at the edge of the loss cone corresponding to an ionospheric altitude of 200 km. After averaging the electron precipitation flux in the loss cone in the equator, the averaged flux in the equator is equivalent to that at the ionospheric altitude (or mirror point) for each local pitch angles from 0 to 90° [*Jordanova et al.*, 1997] according to the Liouville's theorem. That is,

$$j_{iono}(E) = \overline{j_{oc}(E)} \tag{13}$$

By relating the averaged flux in the equator to the flux at the ionospheric altitude (mirror point) at the same energy, it eliminates the complexity of the integration over various sizes of loss cones in the equatorial plane, thus simplifies the calculation of precipitation flux as shown below. The energy flux can be easily determined at the ionospheric altitude ($\sim$ 200 km) assuming "isotropic" condition (as the averaged flux is no long pitch angle dependent):

$$F_E^{diffuse} = \int_{E1}^{E2} \int_{\alpha=0°}^{90°} j_{iono}(E) E \cos\alpha d\Omega dE \tag{14}$$

where Ω is the solid angle of loss cone.

As for the discrete aurora precipitation, the energy flux is computed with a similar method in *Zhang et al.* [2015] as described in Equation (11). Unlike the above approach

and other studies that use MHD parameters to approximate the electron temperature and density and use field-aligned currents from MHD calculation, we obtain these values from the RAM-SCB model near the low altitude boundary and map them to the ionospheric altitude.

Subsequently, with either the MHD or physics-based approach to specifying the auroral precipitation, the precipitation associated conductance is achieved from Equation (8). After combining with the other contributors, we eventually obtain the global distribution of the ionospheric conductance using Equation (7). It should be noted that since the diffuse and discrete auroral precipitation is mapped along magnetic field lines inside the RAM-SCB domain for the physics-based approach, no precipitation is available in the high-latitude polar cap region due to the finite boundary of the ring current model at 6.6 R_e. To avoid the discontinuity near the high-latitude boundary, an exponential decay of the diffuse auroral precipitation flux is spatially enforced along the magnetic latitude towards the pole at the high-latitude boundary. The "skin depth" of the exponential decay is chosen at 5° in latitude.

3. Results

3.1. Overview of the simulated geomagnetic storm event

We simulate a small geomagnetic storm event occurred on January 25-26, 2013 to investigate the effect of electron precipitation on the auroral conductance, and assess the performance of the model implemented with a physics-based electron precipitation loss module, in which two different types of loss rates are utilized. Figure 2 illustrates the solar wind, interplanetary, and geomagnetic conditions during January 25-26, 2013 obtained from OMNIweb. Around 17:00 UT, a sudden enhancement of solar wind dynamic pressure

results in a moderate storm sudden commencement (SSC) indicated by the increase of SYMH index and a weak but isolated substorm injection with AE $\sim$ 250 nT. Around 23:00 UT, a strong southward turning of interplanetary magnetic field (IMF) initiates substantial injections as AE approaches 800 nT, and SYMH index decreases to -30 nT. This injection lasts for only 2 hours. Several intense injections further take place on the date of January 26, 2015 but they act more continuously.

Following these injections, the HOPE instrument, onboard Van Allen Probes-A that orbits near the equator with apogee ($\sim$ 6 R_e) at MLT of 3 during this event, observes predominant increase of electron flux in the midnight-to-dawn sector (Figure 3(a)). The enhancement at around 17:00 UT and 00:00 UT occurs for a wide range of energy from a few eV to tens of keV, supplying important source population to the ring current. Figure 3(b) shows DMSP observations of electron precipitation energy flux along its trajectory across the polar region. The sharp drop of energy flux indicates the equatorward auroral boundary. Two time intervals are compared. The energy flux in the auroral zone at the time of substorm injection ($\sim$ 23:20-23:50 UT, right panel) is increased by an order of magnitude and extends to lower latitudes when compared to that during quite time ($\sim$ 06:25-06:55 UT, left panel). These in-situ observations suggest that substorm injections bring in evident source population into the inner magnetosphere and subsequently give rise to enhanced electron precipitation down to the atmosphere probably owing to the plasma waves excited in the magnetosphere.

We choose a simulation interval from 12:00 UT, January 25 to 12:00 UT, January 26 during which two isolated injections are observed. We examine how the ring current evolves and how the ionospheric electrodynamics is altered following substorm injections.

We compare simulation results using different methods in representing the loss effect of wave-particle scattering with in-situ observations to evaluate the fidelity of the model.

3.2. Inner magnetosphere electron loss due to wave particle interactions

Figure 4 (a-f) displays RAM-SCB simulation results from using "diffusion coefficient method" in the ring current dynamics: (a) the global distribution of the plasmasphere, (b) electron diffusion coefficients associated with whistler-mode hiss and chorus waves, (c) precipitated and (d) trapped electron flux in the equatorial plane, and (e) energy flux and (f) total electron number flux precipitated at the ionospheric altitude during the injection time at 23:50 UT. The cold plasmasphere develops mainly under the control of convective and corotational electric fields. It is nearly symmetrically distributed surrounding the Earth during the pre-storm quiet time (not shown), whereas remarkable plasma erosion takes place starting from the nightside once the convective electric field is enhanced after the solar wind forcing impinges on the magnetosphere, leading to a day-night asymmetric plasmasphere, with a high-density plume formed in the dusk sector (Figure 5 (a)). The innermost plasmapause is pushed as close as 3.5 R_e to the Earth in the midnight-to-dawn sector, resulting in "empty" magnetosphere for the cold population. Hot electrons with energy of tens of keV are injected towards the Earth from the nightside. The electrons mostly drift eastward around the Earth and undergo various acceleration and loss mechanisms, giving rise to temperature anisotropy in their distribution, which then gives free energy for the excitation of whistler-mode waves, such as chorus waves [e.g., *Jordanova et al.*, 2010]. These waves Doppler shifted to the cyclotron frequency of the hot electrons can resonantly interact with and effectively scatter the electrons into the loss cone.

Figure 4 (b) shows pitch angle diffusion rates of hiss waves inside the plasmapause and chorus waves outside the plasmapause. Only representative energy ($\sim$ 9 keV) and pitch angle (52°) are chosen for demonstration. The diffusion rates are clearly high in the low-density region from pre-midnight to pre-noon sector and in the plasmasphere plume region on the afternoon side, indicating that electrons with such energy and pitch angle in these regions is short-living due to strong scattering process by chorus or hiss waves. Therefore, electron precipitation at 9 keV (Figure 4 (c)) is accordingly high in these regions. For example, outside the plasmapause (marked by black dots), precipitation flux is prominent in the midnight-to-noon region through the dawn where chorus waves are probably active after the tail particle injection. Inside the plasmasphere in the dusk sector, significant precipitation also occurs due to the hiss wave scattering. On the other hand, the trapped electrons in Figure 4 (d) mainly appear on the dawn side inside the plasmapause as the scattering loss there is insignificant and in the noon sector outside L of 4 where the pitch angle diffusion coefficients are not so strong. Once the electrons sink down to the atmosphere along magnetic field lines they carry energy source to the upper atmosphere. Figure 4 (e) and (f) show that the ionospheric energy deposit mostly appears around 60° in the region from post-midnight through dawn to the post-noon, while little energy precipitation occurs in the afternoon sector. Such a spatial distribution suggests the dominant role of whistler-mode chorus waves in scattering electrons in the dawn sector, consistent with observations in which whistler-mode chorus waves are found to be likely excited in the dawn sector [*Li et al.*, 2009].

Figure 5 shows simulation results from using the "lifetime method". In Figure 4 (a), a similar asymmetric plasmasphere is developed. The electron lifetime (Figure 4 (b)) is

found to be much shorter outside the plasmapause than that inside the plasmapause at energy of 9 keV, indicating a more efficient scattering loss due to chorus waves outside the plasmapause. The electron flux at 9 keV within the loss cone (Figure 5 (c)) mainly occurs in the pre-midnight to post-dawn sector while little precipitation is produced in the pre-noon to the pre-midnight sector. The peak precipitation appears in the post-midnight region with L from 4 to 6. Meanwhile, the trapped flux (Figure 5 (d)) also shows a similar spatial distribution but with smaller amount of electrons appearing in the afternoon sector than in the dawn sector. The relative low magnitude of trapped electron flux in the afternoon sector is attributed to the short lifetimes of the electrons when they travel eastward from the nightside and are partly lost into the loss cone along their drift path and dayside boundary. While mapping the equatorial precipitation along magnetic field lines down to the ionospheric altitude, the above local-time dependence of precipitation results in ionospheric energy deposit concentrating around latitude of 55° from MLT of 2 to 8 (see Figure 5 (e, f)), but the precipitation flux is rather weak from early morning to pre-midnight sector.

When comparing these two sets of simulation results, the "diffusion coefficient method" not only shows considerably large diffuse precipitation flux in the equator, but also exhibits different spatial distribution. While the "lifetime method" results in electron precipitation confined at a much lower ionospheric latitude, the "diffusion coefficient method" leads to the precipitation at higher latitudes and over a larger coverage in local times.

Since the pitch angle diffusion coefficients adopted in the "diffusion coefficient method" depend on energy, pitch angle and local plasma conditions, Figure 6 displays the pitch angle diffusion coefficients $D_{\alpha\alpha}(E, \alpha)$ in the energy-pitch angle space at L = 5.0 at two

selective MLTs of 8 and 15, where chorus and hiss waves are expected to take a part respectively. It can be seen that the chorus waves can cause rapid scattering for pitch angles below 60° for energies between 10 keV and 100 keV as well as over a larger range of pitch angles for energies below a few keV. These two branches actually correspond to the lower and upper band chorus respectively. The hiss waves on the other hand exert influence over a limited energy range for most pitch angles. As a consequence, the energy spectra of precipitation at these two locations evidently show energy dependence. At MLT of 8, precipitation takes place over a wide range of energies below 100 keV due to chorus wave scattering, while electrons scattering loss at MLT of 15 due to hiss wave scattering is confined within energy range of 30-100 keV at L of 5.0, indicating global asymmetry in the ionospheric precipitation as shown in Figure 4 (e, f).

We further probe the difference/similarity between these two simulations by comparing the trapped electron flux to observations from Van Allen Probes. Figure 7 illustrates the spin-averaged electron flux along the Van Allen Probes-A, which was orbiting near the equatorial plane with the apogee near MLT of 3. The near-equator orbit enables the observation of trapped electrons under current time resolution. In the data, the electron flux suddenly increases around 01:00 UT of Jan 26, 2013, and more plasma injections are observed in the next orbit from 08:00 to 11:00 UT of Jan 26, 2013. From the modeling results, both simulations record the start time of injections at 00:00 UT of Jan 26, 2013, which appears to be one hour earlier than in the observations. In fact, an enhancement is also visible in the data at the same time but with a much smaller intensity. Both simulations show quite similar temporal evolution of the trapped ring current electrons following the initiation of injection, suggesting that the influence of

using different loss methods is very small. In other words, using pitch angle diffusion coefficients is almost equivalent to using lifetimes for solving the trapped electron flux distribution, which unambiguously supports previous studies on radiation belt dynamics that utilize lifetime scales [e.g., *Ripoll et al.*, 2014, 2015, 2016; *Artemyev et al.*, 2015; *Mourenas et al.*, 2012a, b, 2014; *Yu et al.*, 2013; *Yu et al.*, 2014b].

We also compare the simulated precipitation flux to observations from NOAA/POES satellites in Figure 8. POES satellites measure precipitation electron flux with the onboard 0° telescope while traveling along the low Earth polar orbits. Such in-situ observations from six POES satellites are mapped to the magnetic equator, and further binned into L-time diagram for different local time sectors (i.e., MLT of 03-09 and 21-03 in Figure 8 (a, b)). The spatial resolution is chosen at 0.25 R_e between 2.5 and 6.5 R_e and temporal resolution of 0.5 hour. The observed precipitation flux is obtained from 1-20 keV energy channels. The precipitation is found to be rather weak before the storm and is slightly enhanced near L of 6.0 around 17-18 UT after a small injection. It is then largely intensified during substorm injections starting around 23:30 UT. The innermost precipitation penetrates as close as L of 4.5 near the injection peak at 00:30 UT in the nightside and dawn sectors. Precipitation in the "diffusion coefficient method" (Figure 8 (c, d)) tends to occur at larger L shells than in the "lifetime method" (Figure 8 (e, f)) and is in better agreement with the data. It also captures the precipitation before 18:00 UT which is not present in the "lifetime method", but does appear in the data. Furthermore, the "diffusion coefficient method" shows dynamic precipitation from outer region to lower L shells during substorm injections, consistent with observations. However, the magnitude of the precipitation is not as high as in the data, suggesting that the waves may indeed be

stronger in this particular event. There is also a strong burst of precipitation for $4 < L < 5$ jut after 00:30 UT that is present in both models, but not in the data. This may be related to the incorrect location of the predicted plasmapause, or uncertainty in mapping field lines from the equatorial region to the ionosphere in the night sector. We checked plasmasphere electron density inferred from Van Allen Probes data [*Kurth et al.*, 2015] and found that during the injection time (from 00:00 UT to 02:00UT), both spacecraft subsequently pass the midnight plasmapause (chosen at density of 50/cc) that is about 0.5-1.0 R_e further than the plasmapause location in the model. This means that the modeled precipitation flux within $4 < L < 5$ at the "burst" time comes from the region outside the plasmapause while the POES observations display the precipitation flux originated from inside the plasmapause, leading to the disagreement in this region. Therefore, inclusion of a more accurate plasmapause model [*Liu et al.*, 2015] should be one of the future work. In general, the agreement between the new "diffusion coefficient method" and the data is much better than that between the "lifetime method" and the data and represents a prominent improvement. This indicates that the newly implemented electron loss method based on pitch angle diffusion process, a more comprehensive method than the lifetimes, improves the performance of the ring current model in capturing the global spatial distribution and temporal evolution of the electron precipitation. It thus grants a promising tool for studying the integrated magnetosphere-ionosphere physics in the future.

The above results on the trapped and precipitated electrons are actually an manifestation of the underlying loss process to the distribution when applying different loss rates. A distribution initially with larger intensity at larger pitch angles usually finds itself to evolve towards a flatter profile in the pitch angle space, due to diffusion processes. The

direct effect is that the distribution at larger pitch angles is reduced while that at smaller pitch angles increases. This process is what the diffusion coefficients can explain in the model. In contrast, if the lifetimes are applied to the distribution at all pitch angles, the whole distribution is decreased by a certain factor. For the trapped electrons, both methods show similar effect on the distribution. But for the precipitated electrons, owing to the pitch angle diffusion towards lower pitch angles, the precipitation flux is higher than that using lifetimes.

3.3. Ionospheric electrodynamics

We next focus on the ionospheric response following the electron precipitation. In order to manifest this new self-consistent coupling between the auroral precipitation and the ring current dynamics (Figure 1 (b)), we further compare the results with the traditional MHD approach (Figure 1 (a)). Figure 9 shows the ionospheric electric potential, field-aligned currents (FACs), energy flux, and Hall conductance at the ionospheric altitude from using the physics-based approach (top and middle panels) and using MHD approach (bottom panels) at 23:50 UT. As the IMF is southward oriented, the typical two-cell potential/convection pattern and both Region 1 and 2 FACs are well revealed in all of these three simulations.

The ionospheric conductance is a combined effect of diffuse precipitation initiated by pitch angle scattering as described above, the discrete precipitation specified via the upward field-aligned current, the EUV radiation, and polar rain. It is found that with the self-consistent calculation of precipitation from the ring current using pitch angle diffusion coefficient method for the wave-scattered electron loss, the electron energy flux in the ionosphere is largely contributed by the diffuse precipitation due to chorus wave scattering

outside the plasmapause in the post-midnight to dawn sector. The energy deposit in the diffusion coefficient method peaks at a latitude around 62° and further extends to dayside sector. Accordingly, the Hall conductance is regulated mainly by the solar illumination on the dayside and the above diffuse precipitation that forms an aurora oval from the midnight to early morning side. In contrast, with the lifetime method for the ring current electron loss, the precipitated energy flux mainly occurs below 60° in the early morning sector, without extending into the dayside, consistent with the precipitation pattern in the equatorial plane in Figure 5. The Hall conductance is consequently enhanced at lower latitude. On the other hand, the energy flux in the MHD approximation appears as an oval in the ionosphere and it peaks in the dusk-to-midnight sector. This is mainly caused by the large pressure in the dusk magnetosphere as the ring current carries westward drifting protons and is greatly enhanced during substorm time. Subsequently, the auroral Hall conductance is considerably large in the oval, particularly in the dusk-to-midnight sector.

We notice that not only the magnitude but also the spatial distribution of the Hall conductance differ significantly between these two approaches. While verifying the global conductance pattern in the ionosphere is challenging, comparisons with DMSP measurements of precipitated electron energy flux would assist in validating, to a certain extend, the fidelity of the simulated auroral precipitation. Figure 10 illustrates the integrated electron energy flux (from 30 eV to 30 keV) observed along one DMSP trajectory across the southern polar cap during the substorm injection time (black), the simulated energy flux from the kinetic physics-based approach (blue), and MHD approach (green). The two bump-like enhancements of flux in the data represent intense auroral electron

precipitation. The MHD calculation (green) generally captures the location of the peak precipitation in the auroral zone, but it overestimates the peak flux in the dusk sector and the flux at lower latitudes. Too much precipitation flux is observed in the dusk sub-auroral region, mainly because the MHD approach relies on the MHD parameters such as pressure in the model, which is large when the ring current is intensified after substorm injections. On the other hand, the self-consistent physics-based calculation produces an enhancement in the dawn sector near latitude of 60°, and the flux rapidly drops near the auroral boundary, thus in better agreement with the data. But the peak magnitude or the location of peak precipitation in the dawn sector is not well reproduced, indicating that the whistler mode chorus waves in the dawn sector implemented in the diffusion coefficient method is not as strong as in this substorm event. In the dusk sector, the peak precipitation flux is captured, but the location of the peak is missed by a few degree towards lower latitudes than in the data. One possible reason for this mismatch in the physics-based calculation with diffusion loss method could be that the hiss waves employed for the scattering loss in the dusk sector overloads electron precipitation at lower latitudes. Thus more realistic or event-specific hiss-associated diffusion rates may be demanded. Furthermore, more scattering responsible for higher-latitude precipitation outside the plasmapause are also needed in the dusk sector. The large low-latitude precipitation in the simulation may also suggest that the inner magnetosphere experiences less shielding than in reality, causing a penetration of electric field to much lower latitudes. Such discrepancy was previously reported in *Yu et al.* [2015] where the dawn-to-dusk electric field in the dusk sector overly penetrates to the inner region, corresponding to a lower latitude in the ionosphere. A

649 stronger shielding would probably redress the location of the plasmapause boundary and
650 hence the auroral precipitation zone.

4. Discussion and Conclusions

651 We implemented, in the geospace general circulation model, a physics-based diffuse
652 aurora precipitation module for the ionospheric conductivity. It is accomplished by de-
653 termining the differential electron flux within the loss cone in the equatorial region and
654 mapping it down to the ionosphere. This approach enables the coupling of diffuse auroral
655 precipitation of magnetospheric origin to the ionosphere and improves the self consistency
656 of the connection between the ionospheric electrodynamics and magnetospheric dynam-
657 ics. The reason of such effort is because a common but inconsistent approximation has
658 been employed for a long time in global MHD models to estimate the precipitation flux,
659 owing to the incapability of capturing the kinetic precipitation characteristics originated
660 in the inner magnetosphere in these global MHD models. After coupling to a ring current
661 model with magnetospheric particle drift physics, it is possible to have a more physical
662 representation of ionospheric electron precipitation.

663 To resolve the auroral precipitation originated from the wave-particle scattering in the
664 magnetosphere, the effect of wave scattering loss is examined by utilizing either pitch
665 angle diffusion coefficients or lifetimes. The diffusion coefficients, an important indicator
666 of how efficient the particles diffuse in pitch angle space, are determined from the quasi-
667 linear theory and a recent satellite database for wave characteristics, and depend on local
668 plasma density, the energy and pitch angle of electrons, and geomagnetic activity level.
669 In contrast, inferring the electron lifetimes from these diffusion coefficients eliminates the
670 pitch angle dependence, leaving merely the energy dependence for the lifetimes.

We conduct three simulations with the geospace general circulation model: simulation (1) uses the new self-consistent physics-based approach to determining the auroral precipitation in the ring current model which uses new pitch angle diffusion coefficient to represent the scattering effect on electrons; simulation (2) uses the new self-consistent physics-based approach to determining the auroral precipitation in the ring current model which uses electron lifetimes inferred from the above diffusion coefficient for the wave scattering effect; simulation (3) uses the MHD parameters to determine the auroral precipitation without using the precipitation flux from the ring current model but from the MHD model. From these simulations and comparisons with observations, we reach the following conclusions:

1. The diffusion loss method captures the auroral electron precipitation in the region at large L-shells ($5 < L < 6$) in the night and dawn sectors during both quiet and disturbed time. Significant enhancement and penetration of precipitation to low L-shells during the substorm injection time is also reproduced, thus shows reasonable agreement with the dynamics revealed in the NOAA/POES observations.

2. With the diffusion coefficient-based precipitation mechanism, the precipitating energy flux at the ionospheric altitude is dominantly strong in the pre-midnight to dayside through the dawn sector, peaked around 60° latitude. The ionospheric auroral conductance caused by the diffuse electron precipitation is well correlated with the chorus wave outside the plasmapause in the magnetosphere, implying the importance of wave-particle interactions in regulating the ionospheric dynamics.

3. Comparisons with DMSP observations of precipitation energy flux indicates that the chorus wave scattering included in the diffuse model via diffusion coefficients can

mostly explain the diffuse electron precipitation in the dawn sector, such as the enhanced precipitation flux at auroral latitudes and flux drop near the subauroral latitudes. In contrast, the MHD approximation largely overestimates the precipitation flux at lower latitudes.

4. Both diffusion coefficient and lifetime methods show similar temporal evolution of the trapped ring current electrons, but the lifetime method considerably underestimate the intensity of the precipitated ring current electrons in the higher-latitude region, hence agreed worse with NOAA/POES observations than in the diffusion method. This is probably attributed to the fact that lifetimes are independent on pitch angles. When there is a large gradient near the edge of loss cone in the distribution (usually the distribution increases with pitch angle), applying the lifetime to the distribution as a whole reduces the distribution in all pitch angles, leading to smaller precipitation flux within the loss cone. On the other hand, the diffusion coefficients carry full pitch angle information and represent the diffusion in the distribution, which eventually will bring the distribution towards an equilibrium (flatten) stage. Therefore the loss cone precipitation flux is "filled" up after the diffusion process, resulting in more precipitation.

5. While comparing the simulation results with observations, we also identified in the model several shortcomings that require further improvement. For example, in the diffusion coefficient method, the magnitude of precipitation is not as high as in both POES and DMSP observations, suggesting that the waves are probably stronger in the particular substorm event than that derived in the diffusion coefficients. Future studies may consider event-specific wave characteristics to improve the representation of wave scattering loss in the model. In addition, precipitation in the dusk aurora zone is predicted at a lower

latitude than in the data, implying in the model either an overestimate of hiss scattering or a weaker electric field shielding in the inner magnetosphere that is not strong enough to impede the penetration to lower latitudes. Future work will be also focused on coupling the FACs calculated in the ring current model with the ionosphere model, besides the FACs from the MHD model.

In summary, this work marks the first step towards implementing a more self-consistent physics-based approach to obtaining auroral precipitation in global circulation models. We find that the use of diffusion rates based on wave-particle interactions in the magnetosphere generally offers substantial improvement in the electron precipitation maps, and has now reached a level of maturity where it can be integrated into global models that care about ionospheric electrodynamics. Future studies will, with the aid of this new precipitation module, investigate in-depth the influence of the wave-particle interactions in the magnetosphere on the ionospheric conductivity as well as the feedback effects. Nevertheless we need to note that based on some identified issues, more studies are still needed on how to best integrate this approach in global models.

Acknowledgments. The authors thank the OMNIweb from NASA Goddard Space Flight Center for providing the solar wind/interplanetary data and the Kyoto, Japan World Data Center System for providing the SYM-H index and AE-index. The DMSP particle detectors were designed by Dave Hardy of AFRL, and the data is obtained from JHU/APL. The authors are also grateful to NOAA website for providing POES data (http://satdat.ngdc.noaa.gov/sem/poes/). The Van Allen Probes data is obtained from ECT website (http://rbsp-ect.lanl.gov). We also thank Dr. Yue Chen for useful discussion on POES observations. This work was supported by the NSFC Grants 73011501 and

41431071, by the Fundamental Research Funds for the Central Universities, and by the Special Program for Applied Research on Super Computation of the NSFC-Guangdong Joint Fund (the second phase). The work at LANL was conducted under the auspices of the U.S. Department of Energy, with partial support from the Los Alamos National Laboratory Directed Research and Development (LDRD) SHIELDS project, and NASA grants NNH13AW83I, NNH14AX90I, and NAS5-01072. The work at University of Michigan was supported through NSF grant ATM-1242787. The research leading to these results has received funding in part from the European Union Seventh Framework Program (FP7/2007-2013) under grant agreement no 606716 SPACESTORM. Part of these simulations were performed on TianHe-2 at National Supercomputer Center in Guangzhou, China. Data used in the study will be made available upon request by contacting the corresponding author.

References

Albert, J., and Y. Shprits (2009), Estimates of lifetimes against pitch angle diffusion, *Journal of Atmospheric and Solar-Terrestrial Physics*, *71*(16), 1647 – 1652, doi: http://dx.doi.org/10.1016/j.jastp.2008.07.004, toward an Integrated View of Inner Magnetosphere and Radiation Belts.

Albert, J. M. (1999), Analysis of quasi-linear diffusion coefficients, *jgr*, *104*, 2429–2442, doi:10.1029/1998JA900113.

Albert, J. M. (2005), Evaluation of quasi-linear diffusion coefficients for whistler mode waves in a plasma with arbitrary density ratio, *Journal of Geophysical Research: Space Physics*, *110*(A3), doi:10.1029/2004JA010844, a03218.

Artemyev, A. V., D. Mourenas, O. V. Agapitov, and V. V. Krasnoselskikh (2013), Parametric validations of analytical lifetime estimates for radiation belt electron diffusion by whistler waves, *Annales Geophysicae*, *31*, 599–624, doi:10.5194/angeo-31-599-2013.

Artemyev, A. V., O. V. Agapitov, D. Mourenas, V. V. Krasnoselskikh, and F. S. Mozer (2015), Wave energy budget analysis in the Earth's radiation belts uncovers a missing energy, *Nature Communications*, *6*, 8143, doi:10.1038/ncomms8143.

Bortnik, J., R. M. Thorne, and N. P. Meredith (2009), Plasmaspheric hiss overview and relation to chorus, *Journal of Atmospheric and Solar-Terrestrial Physics*, *71*(16), 1636 – 1646, doi:http://dx.doi.org/10.1016/j.jastp.2009.03.023, toward an Integrated View of Inner Magnetosphere and Radiation Belts.

Cao, J. B., et al. (2005), First results of low frequency electromagnetic wave detector of tc-2/double star program, *Annales Geophysicae*, *23*(8), 2803–2811, doi:10.5194/angeo-23-2803-2005.

Chen, M. W., and M. Schulz (2001), Simulations of storm time diffuse aurora with plasmasheet electrons in strong pitch angle diffusion, *jgr*, *106*, 1873–1886, doi:10.1029/2000JA000161.

Chen, M. W., C. L. Lemon, T. B. Guild, A. M. Keesee, A. Lui, J. Goldstein, J. V. Rodriguez, and P. C. Anderson (2015a), Effects of modeled ionospheric conductance and electron loss on self-consistent ring current simulations during the 57 april 2010 storm, *Journal of Geophysical Research: Space Physics*, *120*(7), 5355–5376, doi:10.1002/2015JA021285, 2015JA021285.

Chen, M. W., C. L. Lemon, K. Orlova, Y. Shprits, J. Hecht, and R. L. Walterscheid (2015b), Comparison of simulated and observed trapped and precipitating electron

784 fluxes during a magnetic storm, *Geophysical Research Letters*, *42*(20), 8302–8311, doi:
785 10.1002/2015GL065737, 2015GL065737.

786 De Zeeuw, D. L., S. Sazykin, R. A. Wolf, T. I. Gombosi, A. J. Ridley, and G. Tóth
787 (2004), Coupling of a global MHD code and an inner magnetospheric model: Ini-
788 tial results, *Journal of Geophysical Research (Space Physics)*, *109*, A12219, doi:
789 10.1029/2003JA010366.

790 Fok, M.-C., N. Y. Buzulukova, S.-H. Chen, A. Glocer, T. Nagai, P. Valek, and J. D.
791 Perez (2014), The comprehensive inner magnetosphere-ionosphere model, *Journal of*
792 *Geophysical Research: Space Physics*, *119*(9), 7522–7540, doi:10.1002/2014JA020239,
793 2014JA020239.

794 Fridman, M., and J. Lemaire (1980), Relationship between auroral electrons
795 fluxes and field aligned electric potential difference, *jgr*, *85*, 664–670, doi:
796 10.1029/JA085iA02p00664.

797 Ganushkina, N. Y., O. A. Amariutei, Y. Y. Shprits, and M. W. Liemohn (2013), Transport
798 of the plasma sheet electrons to the geostationary distances, *jgr*, *118*(1), 82–98, doi:
799 10.1029/2012JA017923.

800 Glauert, S. A., and R. B. Horne (2005), Calculation of pitch angle and energy diffusion
801 coefficients with the PADIE code, *Journal of Geophysical Research (Space Physics)*,
802 *110*, A04206, doi:10.1029/2004JA010851.

803 Glauert, S. A., R. B. Horne, and N. P. Meredith (2014), Three-dimensional electron
804 radiation belt simulations using the BAS Radiation Belt Model with new diffusion
805 models for chorus, plasmaspheric hiss, and lightning-generated whistlers, *Journal of*
806 *Geophysical Research (Space Physics)*, *119*, 268–289, doi:10.1002/2013JA019281.

807 Glocer, A., M. Fok, X. Meng, G. Toth, N. Buzulukova, S. Chen, and K. Lin (2013), Crcm
808 + batsrus twoway coupling, *Journal of Geophysical Research: Space Physics*, *118*(4),
809 1635–1650, doi:10.1002/jgra.50221.

810 Horne, R. B., R. M. Thorne, N. P. Meredith, and R. R. Anderson (2003), Diffuse auroral
811 electron scattering by electron cyclotron harmonic and whistler mode waves during
812 an isolated substorm, *Journal of Geophysical Research: Space Physics*, *108*(A7), doi:
813 10.1029/2002JA009736, 1290.

814 Horne, R. B., T. Kersten, S. A. Glauert, N. P. Meredith, D. Boscher, A. Sicard-Piet, R. M.
815 Thorne, and W. Li (2013), A new diffusion matrix for whistler mode chorus waves, *Jour-*
816 *nal of Geophysical Research (Space Physics)*, *118*, 6302–6318, doi:10.1002/jgra.50594.

817 Jordanova, V. K., J. U. Kozyra, G. V. Khazanov, A. F. Nagy, C. E. Rasmussen, and
818 M.-C. Fok (1994), A bounce-averaged kinetic model of the ring current ion population,
819 *Geophys. Res. Lett.,* , *21*, 2785–2788, doi:10.1029/94GL02695.

820 Jordanova, V. K., J. U. Kozyra, and A. F. Nagy (1996), Effects of heavy ions on the
821 quasi-linear diffusion coefficients from resonant interactions with electromagnetic ion
822 cyclotron waves, *Journal of Geophysical Research: Space Physics*, *101*(A9), 19,771–
823 19,778, doi:10.1029/96JA01641.

824 Jordanova, V. K., J. U. Kozyra, A. F. Nagy, and G. V. Khazanov (1997), Kinetic model
825 of the ring current-atmosphere interactions, *Journal of Geophysical Research (Space*
826 *Physics)*, *102*, 14,279–14,292, doi:10.1029/96JA03699.

827 Jordanova, V. K., Y. S. Miyoshi, S. Zaharia, M. F. Thomsen, G. D. Reeves, D. S. Evans,
828 C. G. Mouikis, and J. F. Fennell (2006), Kinetic simulations of ring current evolution
829 during the Geospace Environment Modeling challenge events, *Journal of Geophysical*

Research (Space Physics), *111*, A11S10, doi:10.1029/2006JA011644.

Jordanova, V. K., J. Albert, and Y. Miyoshi (2008), Relativistic electron precipitation by emic waves from self-consistent global simulations, *Journal of Geophysical Research: Space Physics*, *113*(A3), doi:10.1029/2008JA013239.

Jordanova, V. K., R. M. Thorne, W. Li, and Y. Miyoshi (2010), Excitation of whistler mode chorus from global ring current simulations, *jgr*, *115*(A5), doi:10.1029/2009JA014810.

Jordanova, V. K., S. Zaharia, and D. T. Welling (2010), Comparative study of ring current development using empirical, dipolar, and self-consistent magnetic field simulations, *jgr*, *115*, A00J11, doi:10.1029/2010JA015671.

Knight, S. (1973), Parallel electric fields, *planss*, *21*, 741–750, doi:10.1016/0032-0633(73)90093-7.

Kurth, W. S., S. De Pascuale, J. B. Faden, C. A. Kletzing, G. B. Hospodarsky, S. Thaller, and J. R. Wygant (2015), Electron densities inferred from plasma wave spectra obtained by the waves instrument on van allen probes, *Journal of Geophysical Research: Space Physics*, *120*(2), 904–914, doi:10.1002/2014JA020857, 2014JA020857.

Laakso, H., O. Santolik, R. Horne, I. Kolmasov, P. Escoubet, A. Masson, and M. Taylor (2015), Identifying the source region of plasmaspheric hiss, *Geophysical Research Letters*, *42*(9), 3141–3149, doi:10.1002/2015GL063755, 2015GL063755.

Lemon, C., R. A. Wolf, T. W. Hill, S. Sazykin, R. W. Spiro, F. R. Toffoletto, J. Birn, and M. Hesse (2004), Magnetic storm ring current injection modeled with the Rice Convection Model and a self-consistent magnetic field, *Geophys. Res. Lett.*, , *31*, L21801, doi:10.1029/2004GL020914.

Li, L. Y., J. Yu, J. B. Cao, D. Zhang, X. H. Wei, Z. J. Rong, J. Y. Yang, and H. S. Fu (2013), Rapid loss of the plasma sheet energetic electrons associated with the growth of whistler mode waves inside the bursty bulk flows, *Journal of Geophysical Research: Space Physics*, *118*(11), 7200–7210, doi:10.1002/2013JA019109, 2013JA019109.

Li, W., et al. (2009), Global distribution of whistler-mode chorus waves observed on the THEMIS spacecraft, *grl*, *36*, L09104, doi:10.1029/2009GL037595.

Liu, X., W. Liu, J. B. Cao, H. S. Fu, J. Yu, and X. Li (2015), Dynamic plasmapause model based on themis measurements, *Journal of Geophysical Research: Space Physics*, *120*(12), 10,543–10,556, doi:10.1002/2015JA021801, 2015JA021801.

Lotko, W., R. H. Smith, B. Zhang, J. E. Ouellette, O. J. Brambles, and J. G. Lyon (2014), Ionospheric control of magnetotail reconnection, *Science*, *345*(6193), 184–187, doi:10.1126/science.1252907.

Lyons, L. R., D. S. Evans, and R. Lundin (1979), An observed relation between magnetic field aligned electric fields and downward electron energy fluxes in the vicinity of auroral forms, *Journal of Geophysical Research: Space Physics*, *84*(A2), 457–461, doi:10.1029/JA084iA02p00457.

Meredith, N. P., R. B. Horne, and R. R. Anderson (2001), Substorm dependence of chorus amplitudes: Implications for the acceleration of electrons to relativistic energies, *jgr*, *106*, 13,165–13,178, doi:10.1029/2000JA900156.

Meredith, N. P., R. B. Horne, R. M. Thorne, D. Summers, and R. R. Anderson (2004), Substorm dependence of plasmaspheric hiss, *Journal of Geophysical Research: Space Physics*, *109*(A6), doi:10.1029/2004JA010387.

875 Moen, J., and A. Brekke (1993), The solar flux influence on quiet time conductances in
876 the auroral ionosphere, *grl*, *20*, 971–974, doi:10.1029/92GL02109.

877 Mourenas, D., A. Artemyev, O. Agapitov, and V. Krasnoselskikh (2012a), Acceleration
878 of radiation belts electrons by oblique chorus waves, *Journal of Geophysical Research*
879 *(Space Physics)*, *117*, A10212, doi:10.1029/2012JA018041.

880 Mourenas, D., A. V. Artemyev, J.-F. Ripoll, O. V. Agapitov, and V. V. Krasnoselskikh
881 (2012b), Timescales for electron quasi-linear diffusion by parallel and oblique lower-
882 band chorus waves, *Journal of Geophysical Research (Space Physics)*, *117*, A06234,
883 doi:10.1029/2012JA017717.

884 Mourenas, D., A. V. Artemyev, O. V. Agapitov, and V. Krasnoselskikh (2014), Conse-
885 quences of geomagnetic activity on energization and loss of radiation belt electrons by
886 oblique chorus waves, *Journal of Geophysical Research (Space Physics)*, *119*, 2775–2796,
887 doi:10.1002/2013JA019674.

888 Ni, B., R. M. Thorne, Y. Y. Shprits, and J. Bortnik (2008), Resonant scattering of plasma
889 sheet electrons by whistler-mode chorus: Contribution to diffuse auroral precipitation,
890 *Geophysical Research Letters*, *35*(11), n/a–n/a, doi:10.1029/2008GL034032, l11106.

891 Ni, B., R. M. Thorne, R. B. Horne, N. P. Meredith, Y. Y. Shprits, L. Chen, and W. Li
892 (2011a), Resonant scattering of plasma sheet electrons leading to diffuse auroral pre-
893 cipitation: 1. Evaluation for electrostatic electron cyclotron harmonic waves, *Journal*
894 *of Geophysical Research (Space Physics)*, *116*, A04218, doi:10.1029/2010JA016232.

895 Ni, B., R. M. Thorne, N. P. Meredith, R. B. Horne, and Y. Y. Shprits (2011b), Resonant
896 scattering of plasma sheet electrons leading to diffuse auroral precipitation: 2. evalua-
897 tion for whistler mode chorus waves, *Journal of Geophysical Research: Space Physics*,

116(A4), doi:10.1029/2010JA016233, a04219.

Ohtani, S., S. Wing, V. G. Merkin, and T. Higuchi (2014), Solar cycle dependence of nightside field-aligned currents: Effects of dayside ionospheric conductivity on the solar wind-magnetosphere-ionosphere coupling, *Journal of Geophysical Research: Space Physics*, *119*(1), 322–334, doi:10.1002/2013JA019410, 2013JA019410.

Orlova, K., and Y. Shprits (2014), Model of lifetimes of the outer radiation belt electrons in a realistic magnetic field using realistic chorus wave parameters, *Journal of Geophysical Research (Space Physics)*, *119*, 770–780, doi:10.1002/2013JA019596.

Orlova, K., M. Spasojevic, and Y. Shprits (2014), Activity-dependent global model of electron loss inside the plasmasphere, *Geophys. Res. Lett.,* , *41*, 3744–3751, doi:10.1002/2014GL060100.

Pembroke, A., F. Toffoletto, S. Sazykin, M. Wiltberger, J. Lyon, V. Merkin, and P. Schmitt (2012), Initial results from a dynamic coupled magnetosphere-ionosphere-ring current model, *Journal of Geophysical Research: Space Physics*, *117*(A2), n/a–n/a, doi:10.1029/2011JA016979, a02211.

Powell, K. G., P. L. Roe, T. J. Linde, T. I. Gombosi, and D. L. D. Zeeuw (1999), A solution-adaptive upwind scheme for ideal magnetohydrodynamics, *J. Comp. Phys.*, *154*, 284.

Raeder, J., J. Berchem, and M. Ashour-Abdalla (1996), The importance of small scale processes in global MHD simulations: Some numerical experiments, in *The Physics of Space Plasma*, vol. 14, edited by T. Chang and J. Jasperse, MIT Cent. for Theoret. Ceo/Cosmo Plasma PHys., Cambridge, Mass.

Raeder, J., et al. (2001), Global simulation of the Geospace Environment Modeling substorm challenge event, *jgr*, *106*, 381–396, doi:10.1029/2000JA000605.

Rees, M. H. (1963), Auroral ionization and excitation by incident energetic electrons, *Planetary and Space Science*, *11*(10), 1209 – 1218, doi:http://dx.doi.org/10.1016/0032-0633(63)90252-6.

Ridley, A. J., T. I. Gombosi, and D. L. D. Zeeuw (2004), Ionospheric control of the magnetospheric configuration: Conductance, *Ann. Geophys.*, *22*, 567.

Ripoll, J.-F., J. M. Albert, and G. S. Cunningham (2014), Electron lifetimes from narrowband wave-particle interactions within the plasmasphere, *Journal of Geophysical Research (Space Physics)*, *119*, 8858–8880, doi:10.1002/2014JA020217.

Ripoll, J.-F., Y. Chen, J. F. Fennell, and R. H. W. Friedel (2015), On long decays of electrons in the vicinity of the slot region observed by HEO3, *Journal of Geophysical Research (Space Physics)*, *120*, 460–478, doi:10.1002/2014JA020449.

Ripoll, J.-F., et al. (2016), Reproducing the observed energy-dependent structure of Earth's electron radiation belts during storm recovery with an event-specific diffusion model, *Geophys. Res. Lett.,* , *43*, 5616–5625, doi:10.1002/2016GL068869.

Robinson, R. M., R. R. Vondrak, K. Miller, T. Dabbs, and D. Hardy (1987), On calculating ionospheric conductances from the flux and energy of precipitating electrons, *jgr*, *92*, 2565–2569, doi:10.1029/JA092iA03p02565.

Tanaka, T. (2000), The state transition model of the substorm onset, *jgr*, *105*, 21,081, doi:10.1029/2000JA900061.

Tang, B. B., C. Wang, Y. Q. Hu, and J. R. Kan (2011), Intensification of the Cowling current in the global MHD simulation model, *Journal of Geophysical Research (Space*

Physics), *116*, A06204, doi:10.1029/2010JA016320.

Thorne, R. M., B. Ni, X. Tao, R. B. Horne, and N. P. Meredith (2010), Scattering by chorus waves as the dominant cause of diffuse auroral precipitation, *Nature*, *467*, 943–946, doi:10.1038/nature09467.

Tóth, G., et al. (2005), Space Weather Modeling Framework: A new tool for the space science community, *J. Geophys. Res.*, *110*, 12,226, doi:10.1029/2005JA011126.

Tóth, G., et al. (2012), Adaptive numerical algorithms in space weather modeling, *Journal of Computational Physics*, *231*, 870–903, doi:10.1016/j.jcp.2011.02.006.

Tsyganenko, N. A. (1989), A magnetospheric magnetic field model with a warped tail current sheet, *Planet. Space Sci.*, *37*, 5–20, doi:10.1016/0032-0633(89)90066-4.

Vickrey, J. F., R. R. Vondrak, and S. J. Matthews (1981), The diurnal and latitudinal variation of auroral zone ionospheric conductivity, *Journal of Geophysical Research: Space Physics*, *86*(A1), 65–75, doi:10.1029/JA086iA01p00065.

Wei, X. H., et al. (2007), Cluster observations of waves in the whistler frequency range associated with magnetic reconnection in the earth's magnetotail, *Journal of Geophysical Research: Space Physics*, *112*(A10), doi:10.1029/2006JA011771, a10225.

Welling, D. T., V. K. Jordanova, S. G. Zaharia, A. Glocer, and G. Toth (2011), The effects of dynamic ionospheric outflow on the ring current, *Journal of Geophysical Research (Space Physics)*, *116*, A00J19, doi:10.1029/2010JA015642.

Welling, D. T., V. K. Jordanova, A. Glocer, G. Toth, M. W. Liemohn, and D. R. Weimer (2015), The two-way relationship between ionospheric outflow and the ring current, *Journal of Geophysical Research: Space Physics*, *120*(6), 4338–4353, doi:10.1002/2015JA021231, 2015JA021231.

966 Young, D. T., H. Balsiger, and J. Geiss (1982), Correlations of magnetospheric ion com-
967 position with geomagnetic and solar activity, *Journal of Geophysical Research: Space*
968 *Physics*, *87*(A11), 9077–9096, doi:10.1029/JA087iA11p09077.

969 Yu, Y., V. Jordanova, S. Zaharia, J. Koller, J. Zhang, and L. M. Kistler (2012), Validation
970 study of the magnetically self-consistent inner magnetosphere model RAM-SCB, *jgr*,
971 *117*, A03222, doi:10.1029/2011JA017321.

972 Yu, Y., J. Koller, and S. K. Morley (2013), Quantifying the effect of magnetopause shad-
973 owing on electron radiation belt dropouts, *Annales Geophysicae*, *31*, 1929–1939, doi:
974 10.5194/angeo-31-1929-2013.

975 Yu, Y., V. Jordanova, D. Welling, B. Larsen, S. G. Claudepierre, and C. Kletzing (2014a),
976 The role of ring current particle injections: Global simulations and van allen probes
977 observations during 17 march 2013 storm, *Geophysical Research Letters*, *41*(4), 1126–
978 1132, doi:10.1002/2014GL059322.

979 Yu, Y., J. Koller, V. K. Jordanova, S. G. Zaharia, and H. C. Godinez (2014b), Radi-
980 ation belt data assimilation of a moderate storm event using a magnetic field config-
981 uration from the physics-based ram-scb model, *Annales Geophysicae*, *32*(5), 473–483,
982 doi:10.5194/angeo-32-473-2014.

983 Yu, Y., V. Jordanova, S. Zou, R. Heelis, M. Ruohoniemi, and J. Wygant (2015), Mod-
984 eling subauroral polarization streams during the 17 march 2013 storm, *Journal of*
985 *Geophysical Research: Space Physics*, *120*(3), 1738–1750, doi:10.1002/2014JA020371,
986 2014JA020371.

987 Zaharia, S. (2008), Improved Euler potential method for three-dimensional magneto-
988 spheric equilibrium, *Journal of Geophysical Research (Space Physics)*, *113*, A08,221,

989 doi:10.1029/2008JA013325.

990 Zaharia, S., V. K. Jordanova, M. F. Thomsen, and G. D. Reeves (2006), Self-consistent
991 modeling of magnetic fields and plasmas in the inner magnetosphere: Application to a
992 geomagnetic storm, *jgr*, *111*, A11S14, doi:10.1029/2006JA011619.

993 Zaharia, S., V. K. Jordanova, D. Welling, and G. Tóth (2010), Self-consistent inner
994 magnetosphere simulation driven by a global MHD model, *jgr*, *115*, A12,228, doi:
995 10.1029/2010JA015915.

996 Zhang, B., W. Lotko, O. Brambles, M. Wiltberger, and J. Lyon (2015), Electron precip-
997 itation models in global magnetosphere simulations, *Journal of Geophysical Research*
998 *(Space Physics)*, *120*, 1035–1056, doi:10.1002/2014JA020615.

999 Zhima, Z., J. Cao, W. Liu, H. Fu, J. Yang, X. Zhang, and X. Shen (2013), Deme-
1000 ter observations of high-latitude chorus waves penetrating the plasmasphere dur-
1001 ing a geomagnetic storm, *Geophysical Research Letters*, *40*(22), 5827–5832, doi:
1002 10.1002/2013GL058089, 2013GL058089.

Table 1. Three simulations using different methods of calculating the auroral precipitation and ring current electron loss due to wave particle interactions.

Three simulations	auroral precipitation	ring current electron loss
I	physics-based calculation of precipitation	diffusion coefficients for electron loss
II	physics-based calculation of precipitation	lifetimes for electron loss
III	MHD approximation of precipitation	diffusion coefficients for electron loss

Figure 1. (a) The old modeling framework of coupling the global MHD model with the ionospheric potential solver. Within it, the auroral electron precipitation needed in calculating the ionospheric conductance is passed from the MHD model with approximation. (b) The new modeling framework in this study by taking the auroral precipitation from the kinetic ring current model that solves particle distribution functions with pitch angle dependence. This new implementation indicates a physics-based calculation of electron precipitation than the MHD parameterization in the current framework. (c) The specific modeling framework used in this study: global MHD model BATS-R-US, coupled with kinetic ring current model RAM-SCB, and the ionospheric potential solver RIM. The dashed line indicates the new implementation in this study of auroral particle precipitation passing from the ring current model to the ionospheric electrodynamics.

Figure 2. Solar wind, interplanetary and geomagnetic conditions during the moderate magnetic storm event occurred on January 25-26, 2013. The data is obtained from OMNIWeb.

Figure 3. (a) Van Allen Probes-A observations of spin-averaged electron flux from ECT-HOPE (lower panel) and MagEIS instrumentation (upper panel). The displayed energy range covers from 100 eV to 2000 keV. (b) Energy flux observed by DMSP satellite along two trajectories across the polar region of southern hemisphere. The left panel shows energy flux during a quiet time period while the right one is under a disturbed condition.

Figure 4. Simulation results using the wave-particle pitch angle scattering diffusion coefficients (a, b, c, d) are in the equatorial plane, and (e, f) are at the ionosphere altitude. (a) Plasmasphere electron density, (b) bounce-averaged pitch angle diffusion coefficient for energy of 9 keV and pitch angle of 52°, (c) precipitated and (d) trapped electron flux at energy of 9 keV, (e) energy flux, and (f) total number flux at the ionospheric altitude. The black dots in (c), (e), and (f) denote the plasmapause boundary. These global distribution maps are chosen from the time of January 26, 00:50 UT.

Figure 5. Simulation results using electron lifetime, in the same format as in Figure 4. (a) Plasmasphere electron density,(b) lifetime (in hours) for electrons in energy of 9 keV, (c) precipitated and (d) trapped electron flux at energy of 9 keV, (e) energy flux and (f) total number flux at the ionospheric altitude.

Figure 6. Top panels: Bounce-averaged pitch angle diffusion coefficients as function of energy and pitch angle for chorus waves (left) and hiss waves (right) at L of 5 and MLT of 8 and 15 respectively. Bottom panels: Energy spectra of electron precipitation flux at MLT of 8 (left) and 15 (right) for four locations (L=3.0, 4.0, 5.0, 6.0). These plots are chosen at time of 23:50 UT, the same time as in Figure 4.

Figure 7. Trapped population: (a) Van Allen Probes-A observation of spin-averaged electron flux from ECT/MagEIS instrument for $30 \leq E \leq 400keV$. (b) Simulated electron omni flux using diffusion coefficient method. (c) Simulated electron omni flux along the same trajectory using lifetime method. The flux unit is in $1/cm^2/s/sr/keV$.

Figure 8. Precipitated population: (a,b) Observation: six NOAA/POES observation of precipitating energy flux binned in radial distance L and time for two local sectors (03-09 MLT and 21-03 MLT). The spatial resolution in L is 0.25 R_e and the temporal resolution is 30 minutes. (c, d) Diffusion coefficient method result: precipitating energy flux in the same format, using pitch angle diffusion coefficients to represent the wave-particle scattering loss. (e, f) Lifetime method result: precipitating energy flux in the same format, using electron lifetime to account for the wave-particle scattering loss.

Figure 9. Top row: simulation results using the diffusion coefficient loss method and new physics-based calculation of auroral precipitation. Middle row: simulation results using the lifetime loss method and new physics-based calculation of auroral precipitation. Bottom row: simulation results using MHD approximation of auroral precipitation. From left to right columns: ionospheric electric potential, field-aligned currents, energy flux, and Hall conductance above 50° magnetic latitude. The energy flux is plotted in logarithm scale.

Figure 10. Top panel: DMSP F18 trajectory across the southern hemisphere from the dawn to dusk. Bottom panel: observed (black) and simulated (blue, green) energy flux along the satellite trajectory. The blue trace shows the simulation result from using diffusion coefficients in the wave-driven precipitation and the green trace from the simulation using the MHD approximation in the auroral precipitation.

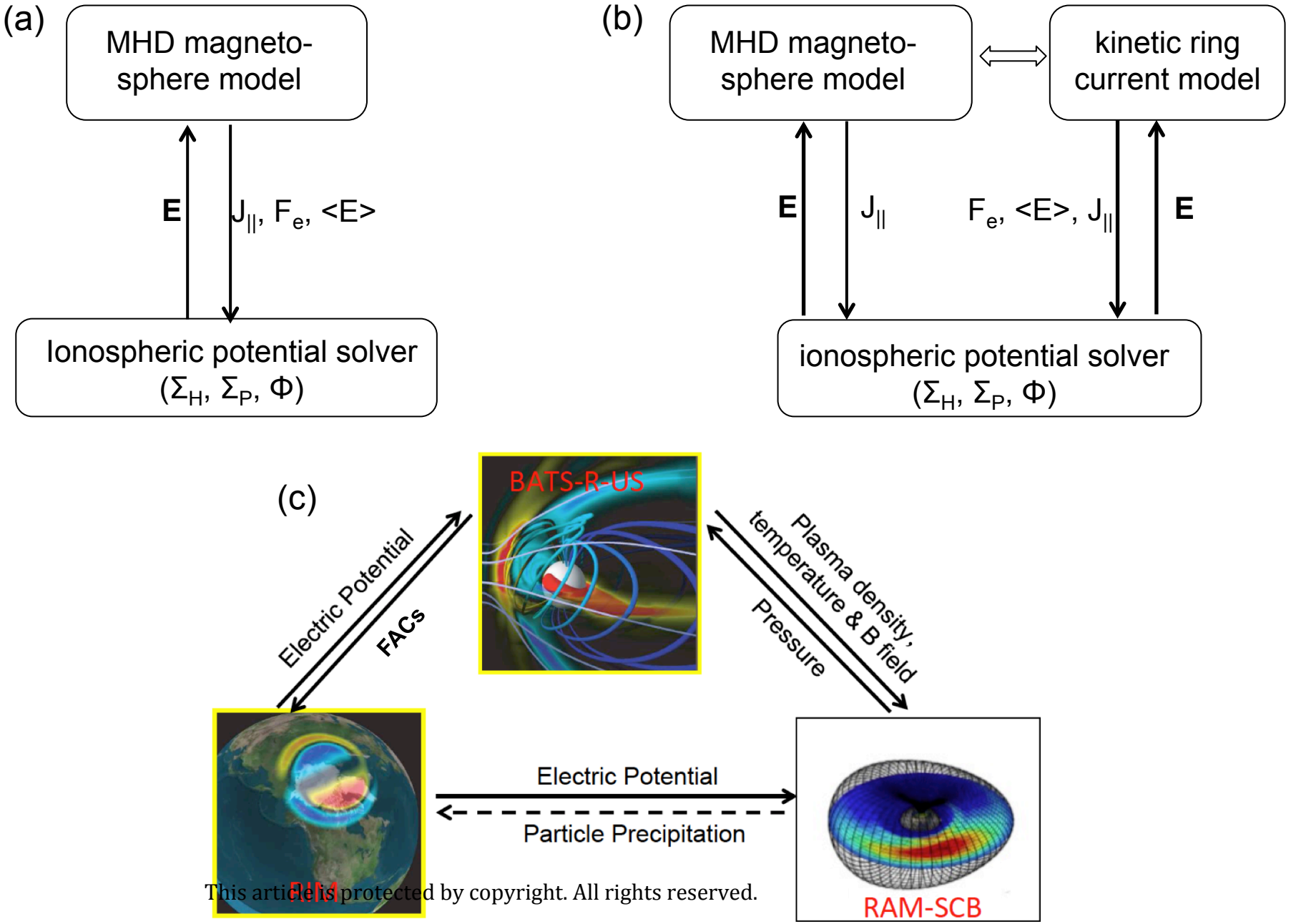

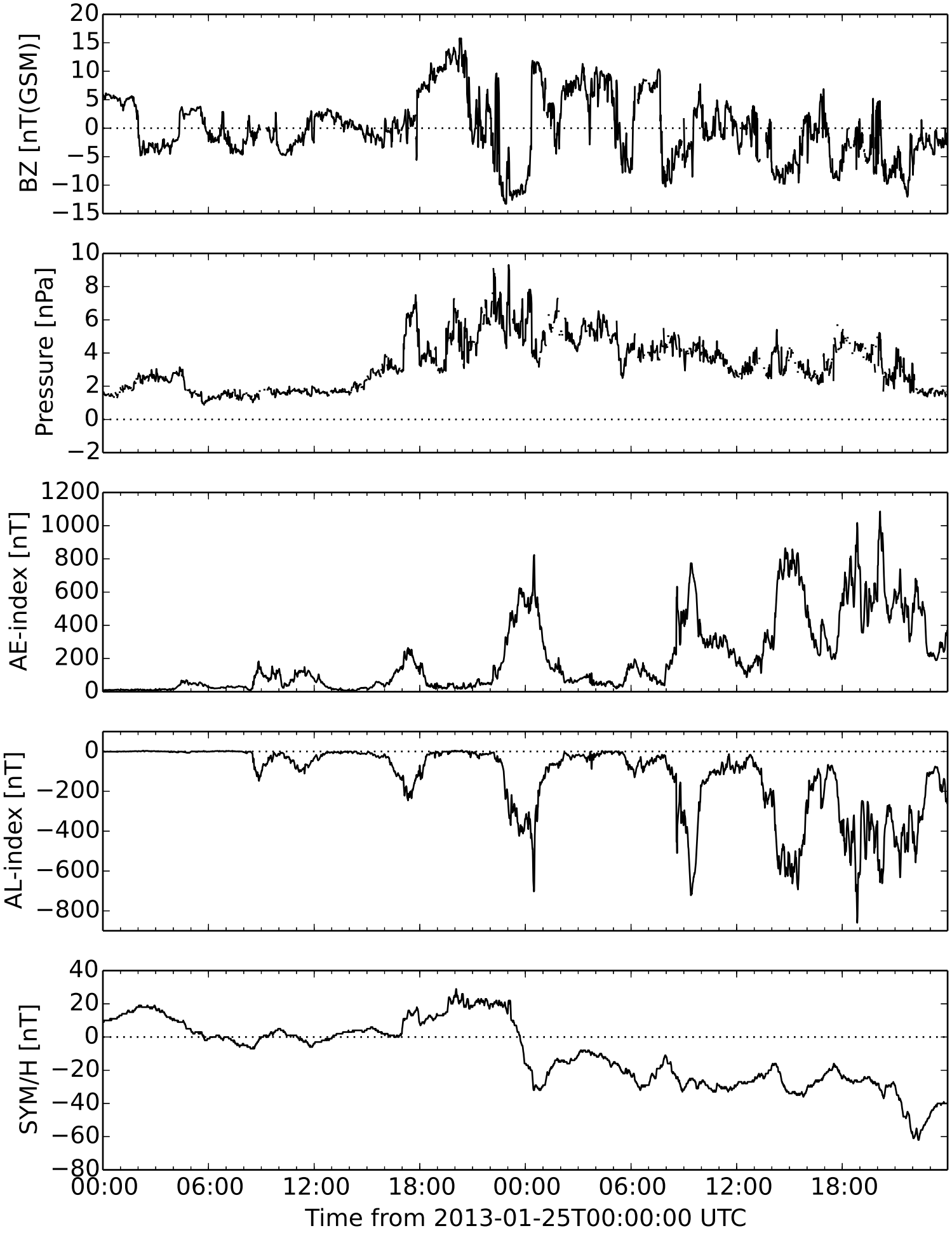

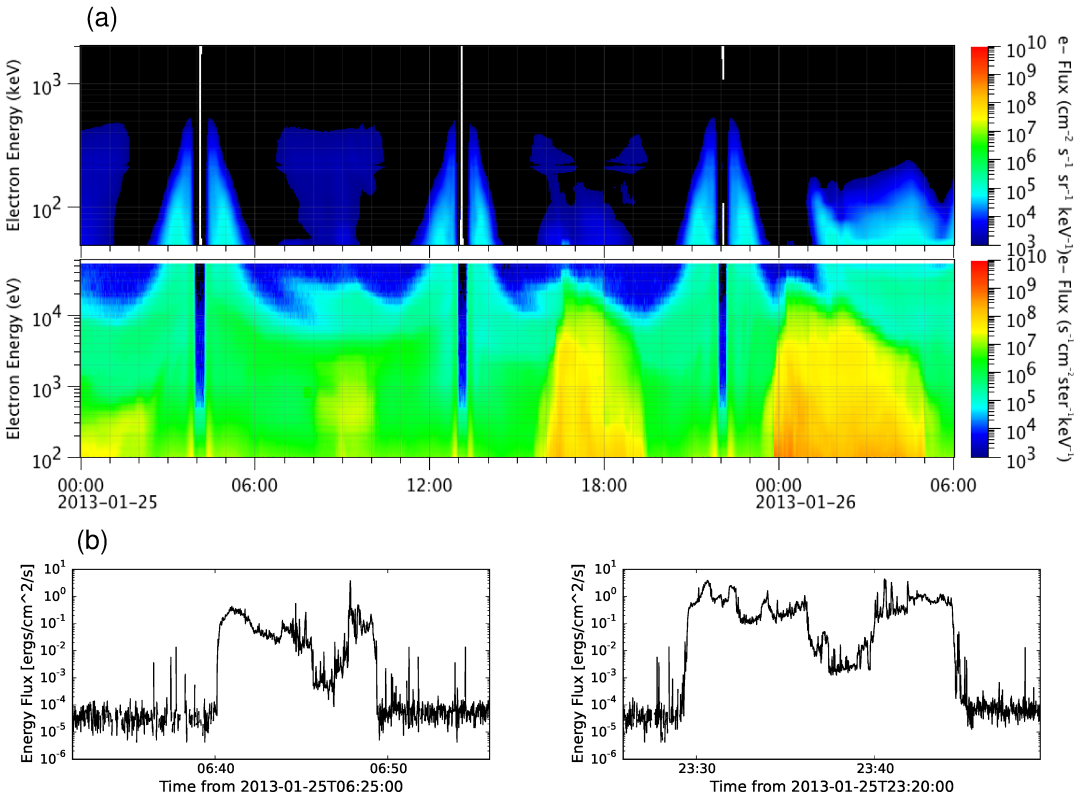

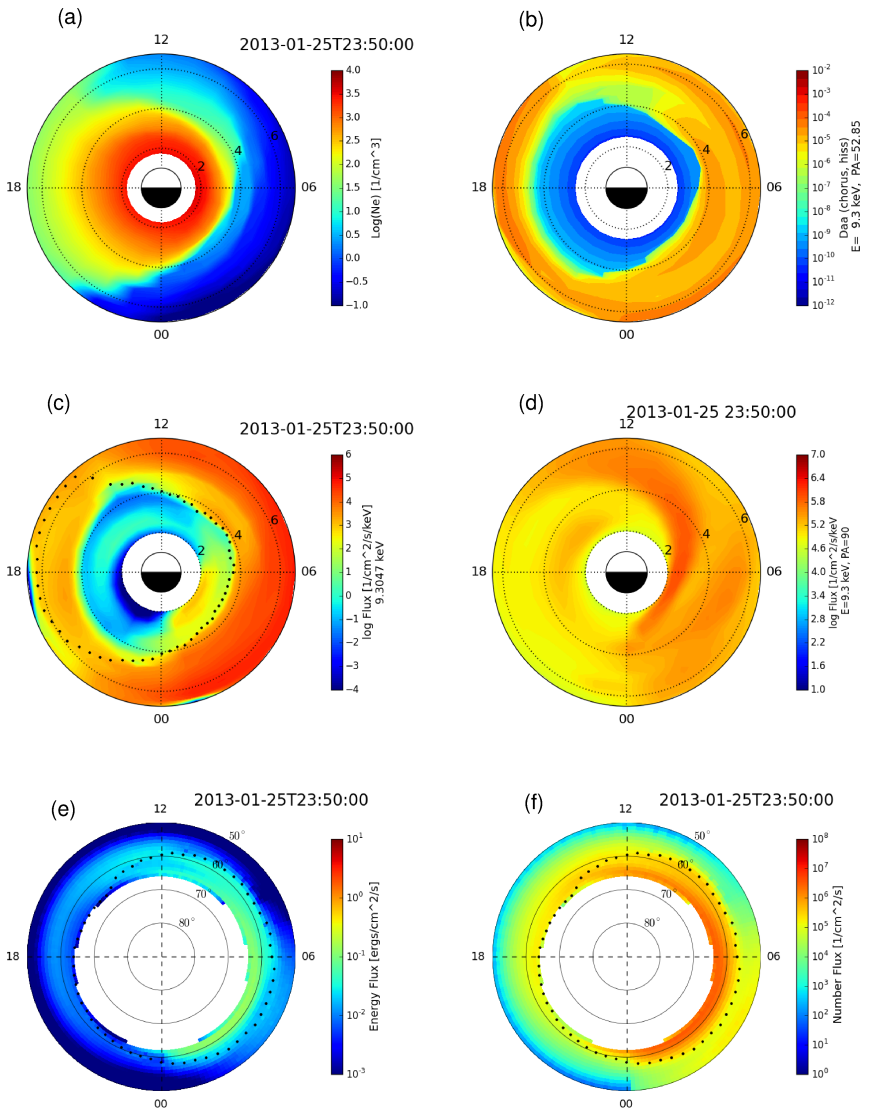

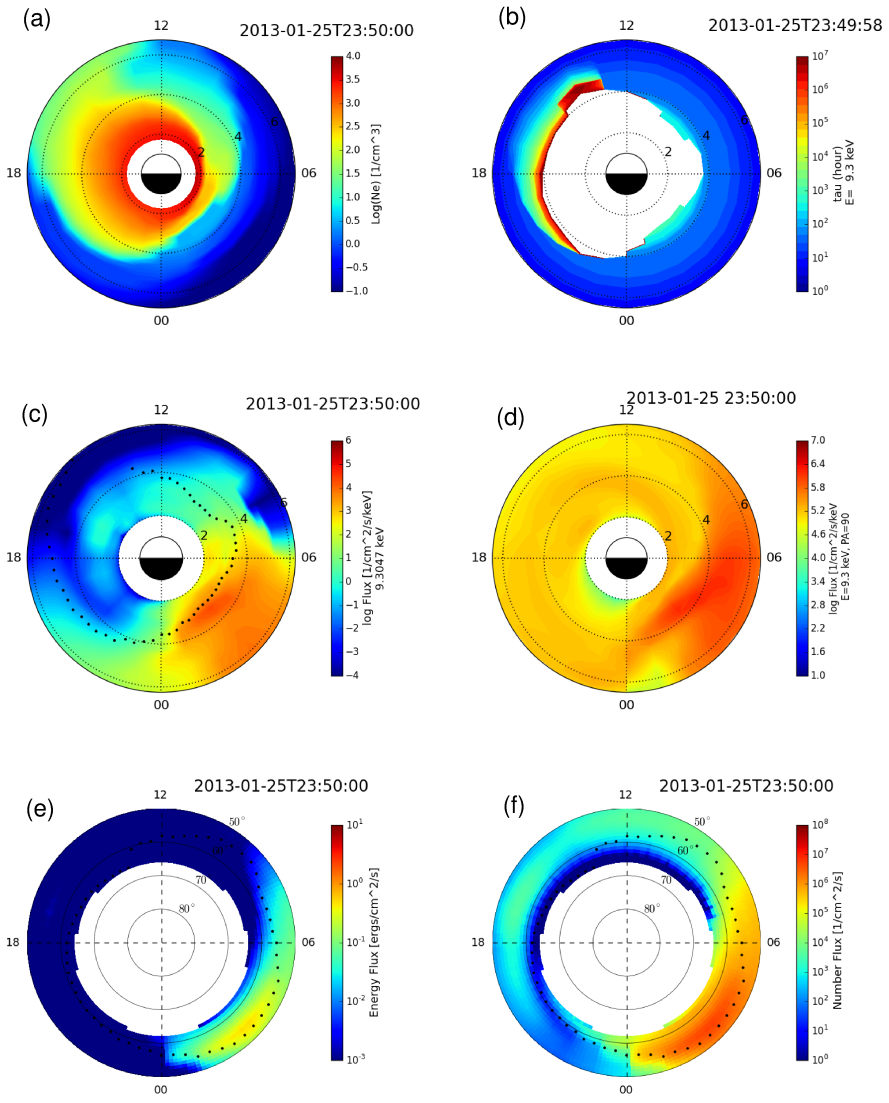

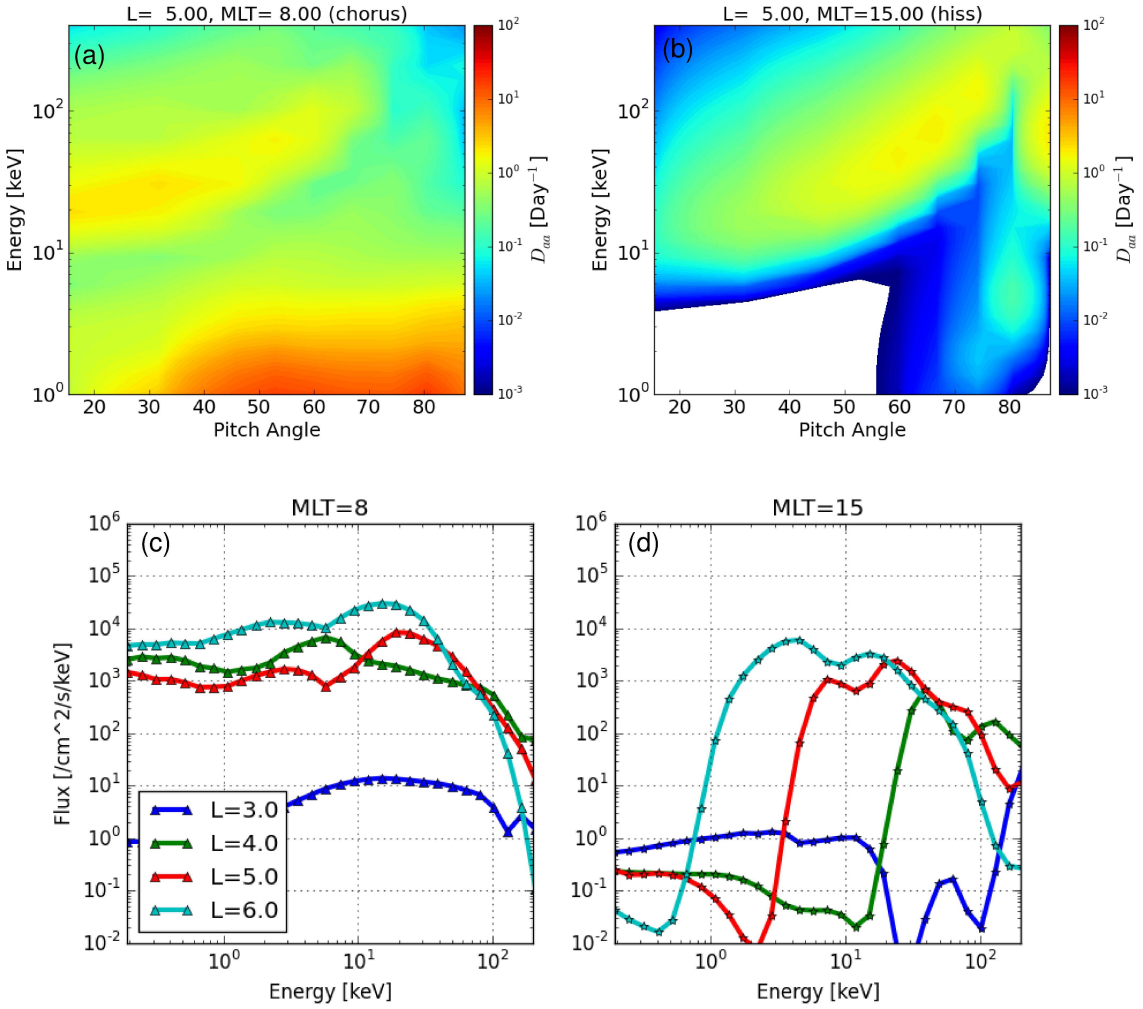

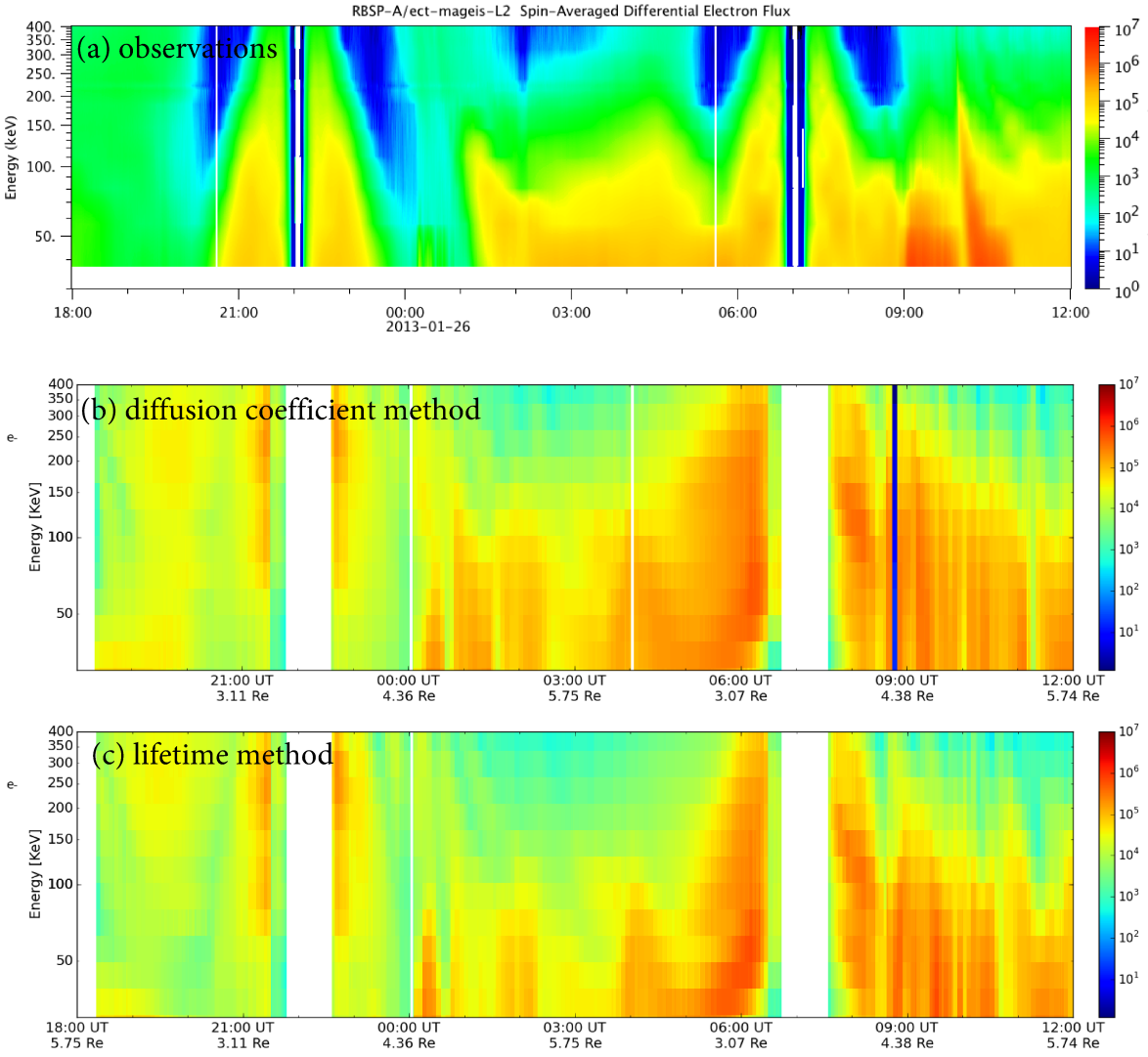

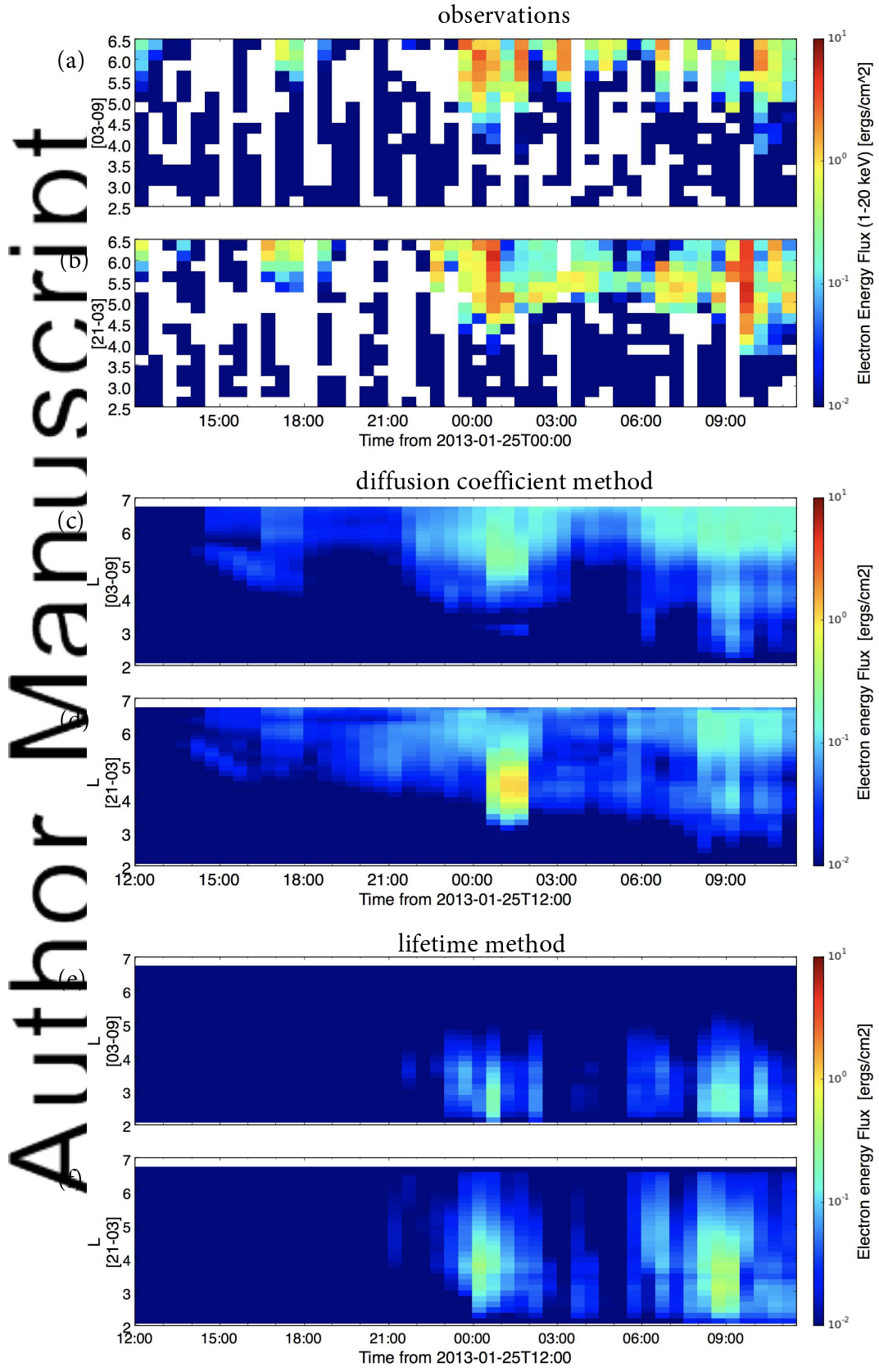

I. Physics-based calculation of precipitation -- diffusion coefficient method

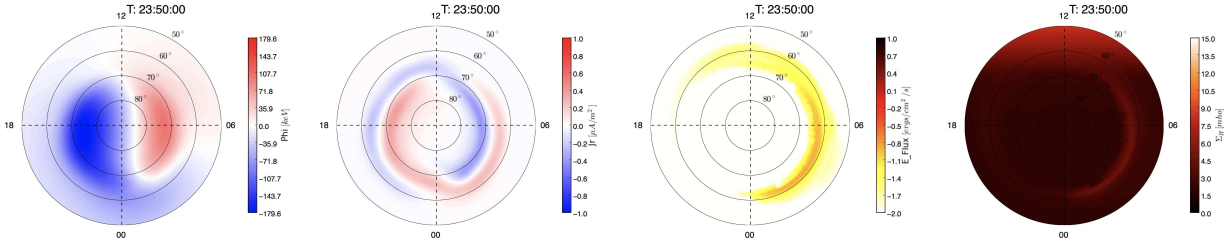

II. Physics-based calculation of precipitation -- lifetime method

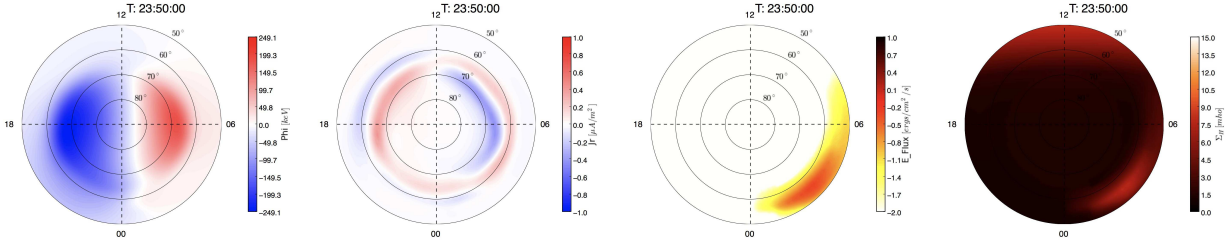

III. MHD approximation of precipitation